Fraunhofer Institut
Techno- und
Wirtschaftsmathematik

I. Ginzburg, K. Steiner

Lattice Boltzmann Model for Free-Surface flow and Its Application to Filling Process in Casting

Berichte des Fraunhofer ITWM, Nr. 34 (2002)

ISSN 1434-9973

Bericht 34 (2002)

Die Veröffentlichungen in der Berichtsreihe des Fraunhofer ITWM können bezogen werden über:

Fraunhofer-Institut für Techno- und
Wirtschaftsmathematik ITWM
Gottlieb-Daimler-Straße, Geb. 49

67663 Kaiserslautern

Telefon: +49 (0) 6 31/2 05-32 42
Telefax: +49 (0) 6 31/2 05-41 39
E-Mail: info@itwm.fhg.de
Internet: www.itwm.fhg.de

Vorwort

Das Tätigkeitsfeld des Fraunhofer Instituts für Techno- und Wirtschaftsmathematik ITWM umfasst anwendungsnahe Grundlagenforschung, angewandte Forschung sowie Beratung und kundenspezifische Lösungen auf allen Gebieten, die für Techno- und Wirtschaftsmathematik bedeutsam sind.

In der Reihe »Berichte des Fraunhofer ITWM« soll die Arbeit des Instituts kontinuierlich einer interessierten Öffentlichkeit in Industrie, Wirtschaft und Wissenschaft vorgestellt werden. Durch die enge Verzahnung mit dem Fachbereich Mathematik der Universität Kaiserslautern sowie durch zahlreiche Kooperationen mit internationalen Institutionen und Hochschulen in den Bereichen Ausbildung und Forschung ist ein großes Potenzial für Forschungsberichte vorhanden. In die Berichtreihe sollen sowohl hervorragende Diplom- und Projektarbeiten und Dissertationen als auch Forschungsberichte der Institutsmitarbeiter und Institutsgäste zu aktuellen Fragen der Techno- und Wirtschaftsmathematik aufgenommen werden.

Darüberhinaus bietet die Reihe ein Forum für die Berichterstattung über die zahlreichen Kooperationsprojekte des Instituts mit Partnern aus Industrie und Wirtschaft.

Berichterstattung heißt hier Dokumentation darüber, wie aktuelle Ergebnisse aus mathematischer Forschungs- und Entwicklungsarbeit in industrielle Anwendungen und Softwareprodukte transferiert werden, und wie umgekehrt Probleme der Praxis neue interessante mathematische Fragestellungen generieren.

Prof. Dr. Dieter Prätzel-Wolters
Institutsleiter

Kaiserslautern, im Juni 2001

Lattice Boltzmann Model for Free-Surface flow and Its Application to Filling Process in Casting

Irina Ginzburg[1] and Konrad Steiner

Fraunhofer Institut für Techno- und Wirtschaftsmathematik, Gottlieb-Daimler-Strasse 49, Kaiserslautern, D-67663, Germany

Received June ??, 2001

A generalized lattice Boltzmann model to simulate free-surface is constructed in both two and three dimensions. The proposed model satisfies the interfacial boundary conditions accurately. A distinctive feature of the model is that the collision processes is carried out only on the points occupied partially or fully by the fluid. To maintain a sharp interfacial front, the method includes an anti-diffusion algorithm. The unknown distribution functions at the interfacial region are constructed according to the first order Chapman-Enskog analysis. The interfacial boundary conditions are satisfied exactly by the coefficients in the Chapman-Enskog expansion. The distribution functions are naturally expressed in the local interfacial coordinates. The macroscopic quantities at the interface are extracted from the least-square solutions of a locally linearized system obtained from the known distribution functions. The proposed method does not require any geometric front construction and is robust for any interfacial topology. Simulation results of realistic filling process are presented: rectangular cavity in two dimensions and Hammer box, Campbell box, Sheffield box, and Motorblock in three dimensions. To enhance the stability at high Reynolds numbers, various upwind-type schemes are developed. Free-slip and no-slip boundary conditions are also discussed.

Key Words: lattice Boltzmann models; free-surface phenomena; interface boundary conditions; filling processes; injection molding; volume of fluid method; interface boundary conditions; advection-schemes; upwind-schemes.

1. INTRODUCTION

Numerical modeling of moving interfaces between immiscible fluids is important for many industrial applications. Solving the incompressible Navier-Stokes equations for two-phase flows is a difficult problem since pressure and velocity derivatives

[1]Author to whom correspondence should be addressed. Email: ginzburg@itwm.fhg.de

may have discontinuities at the interfaces. In addition, a description of the interface motion itself represents a complicated task. Existing methods to treat sharp interfacial problems belong to two main categories: *surface tracking*, a Lagrangian method, and *surface capturing*, an Eulerian one. The former approach explicitly treats the interface as a discontinuity and often the computational mesh directly tracks the interfaces. The latter one does not consider the exact interface position in the discretization of the governing equations, but takes it into account during the interface advection. These two methods can be combined together in some way when the grids are aligned with the interface (*e.g.*, [16, 21, 42, 54, 56, 74]). Excellent overviews on various methods to treat interfaces are given by Unverdi and Tryggvason [81], Sussman and Smereka [79], Rider and Kothe [68], Kothe [47], Rudman [69, 70], and Scardovelli and Zaleski [75].

Free-surface phenomena are ubiquitous in nature and in many industrial applications. Metal casting is such an example. In this case, the density ratio between the melt metal and the air is of such a disparity that the influence of the air on the melt metal can be ignored. Hence the problem of two-fluid flow with interfaces reduces to the problem of one-fluid flow with free-boundaries. The formulation of the free-boundary flow avoids the steep variations of physical quantities in the interfacial region. Several methods to treat the free-surface problem have been developed. Among volume tracking methods, the most popular one is a volume of fluid (VOF) method due to Hirt and Nicholls [34]. This method has been successfully applied to simulate mold filling with regular grids [1, 2, 35, 53], and has been extended to unstructured grids (*e.g.*, [16, 60, 61, 65, 80]). The free Lagrangian method of Fyfe *et al.* [14] and the grid free smoothed particle hydrodynamics (SPH) methods [10, 58] are representative examples of the extension of front tracking methods to treat free-surface problems. In the former case, the computational grid itself is advected by the Lagrangian equations. Whereas in the latter case, the interface is represented by a set of particle positions. A front tracking technique has also been applied to strongly deformable geometries by Galaktionov *et al.* [15]. A review on free-surface methods based on their applicability to the simulations of the mold filling process is given by Kothe *et al.* [48].

Intended for solving the Navier-Stokes equation, the lattice Boltzmann (LB) models [32, 38] do not involve any global linear or nonlinear systems of equations. Their locality and linearity with respect to computational mesh are absolutely essential for the applications of interfacial problems where the conventional CFD solvers may fail to because of the stiffness and/or large dimensions of the problem. Furthermore, the kinetic nature of the LB method provides the physical basis to deal with such complicated physical phenomena as fluids segregation, diffusion, wetting, evaporation, *etc.*, in a elegant manner. A comparison of two-phase Lattice Boltzmann and VOF methods is available in [76]. An extensive literature on the LB multi-phase and multi-component models can be found in [8, 31, 55, 71, 72].

One early LB model for immiscible fluids has been proposed by Gunstensen and Rothman [27]. In this immiscible lattice Boltzmann (ILB) model, the collision and propagation rules are modified on interfacial grid points in order to introduce the desirable interfacial behavior. The ILB model of Gunstensen and Rothman has been originally designed to simulate flows of two immiscible fluids differentiated only by their colors. In addition to the usual collision and advection steps, the ILB

model has an additional "recoloring" step, which preferentially redirects each fluid to the neighboring sites of the same color. This step is accomplished by computing the gradient of the local mass fraction. The "recoloring" step must also preserve the conservation laws. This "recoloring" scheme actually mimics a mechanism of segregation among the two components marked by their colors. Owing to the explicit nature of the LB algorithms, the LB models has difficulty to deal with fluids with large density ratio. In addition, the effective interface boundary conditions implicitly imposed by the LB multi-phase methods have not been given sufficient attention in the past (cf. [18]). The purpose of this paper is to propose a new volume tracking LB method to simulate hydrodynamics with free-surfaces. It can be seen as a modified immiscible lattice Boltzmann model in which one species is the fluid and the other one is considered as vacuum. The proposed LB method is applied to simulate the process of filling a die cavity in metal casting [16, 28, 53], which is a crucial step in casting process since it determines the quality of the final product.

The new LB method is different from the existing LB multi-phase and multi-component models because the collision only occurs on the "active" cells which are fully or partially filled with fluid. The mass fraction of a cell filled with fluid, which is between zero and one, is an additional variable used in the method. A "recoloring operator", similar to that in the ILB models, determines the redistribution of fluid mass carried by each particle population. The macroscopic variables propagate together with the particle distribution functions in the advection step, according to the usual LB evolution equation. The unknown particle distributions at the front of free-surfaces, which cannot be obtained by the usual LB method, are constructed by using the first order Chapman-Enskog expansion of the distribution functions. The free-surface boundary conditions are directly met by matching the coefficients of the series solutions of the distribution functions with the boundary conditions. Due to the rotational invariance, the first-order Chapman-Enskog solutions of the distribution functions are naturally expressed in a local coordinates which are normal and tangent to the free-surface. Therefore the curvilinear interfacial boundaries can be handled easily without reconstruction of mesh geometries.

The solutions for the distribution functions at free-surface are completely specified by the local hydrodynamic variables, *i.e.*, the fluid density and velocity, in two dimensions. In three dimensions, derivatives of velocity tangential to the free-surface are also needed to determine the solutions. The hydrodynamic variables at the free-surface nodes are not determined, however, until all the distributions in a given cell are obtained. The idea here is to derive the hydrodynamic information at free-surface locally, from the *known populations* arriving at a given front node from the neighboring active nodes. In such a way, the resulting solution for unknown distributions at front nodes is implicitly expressed in the form of a linearized function of the known distributions. We obtain unknown quantities from the local least-square solution of a linearized system. This approach follows the basic philosophy of the local second order boundary (LSOB) method [19] where all first and second order momentum derivatives, necessary to impose Dirichlet boundary conditions, are extracted from locally known populations. Therefore, the proposed method is entirely based on a self-consistent kinetic theory, the Chapman-Enskog analysis being consistently applied in the solid and interface boundary regions.

The lattice Boltzmann equation used here is based on the framework of the generalized lattice Boltzmann equation (GLBE) due to d'Humières [38]. In this approach, the collision operator is computed in the space spanned by a basis in momentum space. The basis is presented in a unique form [20], and is suitable for any $DdQb$ model in d dimensions with q velocities [67]. In particular, we present the method in this paper using $D2Q9$ and $D3Q15$ models as examples in two and three dimensions, respectively. The boundary conditions at fluid-solid interfaces are realized by using local reflections of the distribution functions in the spirit of the bounce-back scheme for the no-slip boundary condition. Because the effective accuracy of bounce-back and specular reflections to model no-slip/free-slip boundary conditions (or their combination) depends on the actual choice of all eigenvalues of the collision operator [17, 39], we pay a special attention to address this issue. We also pay special attention to the stability of the LB method [51]. Like any LB model, the method develops instabilities at high Reynolds numbers, even if the free eigenvalues are chosen to improve the stability (cf. [51]). This leads us to design schemes with better stability characteristics. Although upwind approach is widely used in finite-difference/finite-elements schemes, it has not yet been adapted for Lattice-Bolzmann methods. Indeed, one of the merits of the LB methods is that their numerical diffusion (at least at second order) is already accounted in the diffusion coefficient. We show using linear convective-diffusion problem as an example that higher order terms in Chapman-Enskog expansion can introduce negative numerical diffusion into the scheme. In order to compensate it, artificial numerical diffusion can be added. In so far, various upwind LB schemes are constructed in [22], in analogy to one-dimensional upwind [9], full-upwind, and streamline-type multi-dimensional upwind schemes [3]. In the present work, we use the most crude but robust *explicit upwind* approach for free interface simulations at high Re numbers.

The paper is structured as follows. In Section 2, the LB framework and basic macroscopic relations are given. In Section 3.1, first order Chapman-Enskog expansion at interface is presented. In Section 3.2, interface advection with recoloring step is discussed. Reconstruction of unknown populations at the interface is described in Section 3.3. Brief outline of the numerical algorithm is given in Section 3.4. Boundary conditions are discussed in Section 4. Overview of the algorithm is in Section 5. Explicit upwind scheme is discussed in Section 6. Section 7 considers the different aspects of the algorithm using 2D cavity filling and benchmark 3D simulations in injected molding. Concluding remarks are in Section 8. Details to implementation of generalized LB equation are sketched in Appendix A.

2. BASIC THEORY OF LATTICE BOLTZMANN EQUATION

2.1. Lattice Boltzmann Equation

The lattice Boltzmann equation (LBE) is often written in the following form [78]

$$\tilde{N}_i(\boldsymbol{r},t) = N_i(\boldsymbol{r},t) + \sum_{j=0}^{b_m} \mathsf{A}_{ij}[N_j(\boldsymbol{r},t) - N_j^{\mathrm{eq.}}(\boldsymbol{r},t)] + t_p^{\star}(\boldsymbol{C}_i \cdot \boldsymbol{F}) \,, \qquad \text{(1a)}$$

$$N_i(\boldsymbol{r}+\boldsymbol{C}_i, t+1) = \tilde{N}_i(\boldsymbol{r},t) \,, \qquad i \in \{0,\ldots,b_m\} \,, \qquad \text{(1b)}$$

where N_i is the population of the particle moving with D-dimensional velocity $\boldsymbol{C}_i$ ($\boldsymbol{C}_0$ is a zero vector), A is the collision matrix, $\boldsymbol{F}$ is an external force; weight coefficient $t_p^\star$ depends on the discrete velocity set $\boldsymbol{C}_i$, and the index p is equal to c_i^2, ($c_i^2 = \|\boldsymbol{C}_i\|^2$). Equilibrium function $\mathbf{N}^{\mathrm{eq.}}$ is introduced by equation (10) and the coefficients $t_p^\star$ are given in Table 1. They satisfy the following equations:

$$\sum_{i=1}^{b_m} t_p^\star C_{i\alpha}^2 = 1 \ , \quad \forall\alpha = 1, \ldots, D \ , \quad \text{and} \quad t_0^\star = 3 - \sum_{p\neq 0} t_p^\star \ . \tag{2}$$

There are two essential steps in Eq. (1a): *collision* (a) and *propagation* (b). Density ρ and momentum $\boldsymbol{j}$ are defined as

$$\rho(\boldsymbol{r}, t) \ = \ \sum_{i=0}^{b_m} N_i(\boldsymbol{r}, t) \ , \tag{3a}$$

$$\boldsymbol{j}(\boldsymbol{r}, t) \ = \ \boldsymbol{J} + \frac{1}{2}\boldsymbol{F} \ , \quad \boldsymbol{J} = \sum_{i=1}^{b_m} N_i(\boldsymbol{r}, t)\boldsymbol{C}_i \ . \tag{3b}$$

The reason to modify the momentum in the presence of the forcing term is discussed in Section 4, and can also be found in a number of references [4, 17, 39, 49]. The mass and momentum conservation laws impose the following conditions on the collision matrix A:

$$\mathsf{A} \cdot \mathbf{1} = \mathsf{A} \cdot \mathbf{C}_\alpha = \mathbf{0} \ , \qquad \forall\alpha = 1, ..., D \ . \tag{4}$$

where $\mathbf{1} = \{1, \ldots, 1\}$, and the $(b_m + 1)$-vector $\mathbf{C}_\alpha$ is built from the components of the $(b_m + 1)$ population velocities in direction α.

TABLE 1
Equilibrium weights $t_p^\star$ and $r_p^\star$

Model	$t_0^\star$	$t_1^\star$	$t_2^\star$	$t_3^\star$	$r_0^\star$	$r_1^\star$	$r_2^\star$	$r_3^\star$
$D2Q9$	$\frac{4}{3}$	$\frac{1}{3}$	$\frac{1}{12}$	–	$\frac{3-5c_s^2}{3}$	$\frac{c_s^2}{3}$	$\frac{c_s^2}{12}$	–
$D3Q15$	$\frac{2}{3}$	$\frac{1}{3}$	–	$\frac{1}{24}$	$\frac{3-7c_s^2}{3}$	$\frac{1c_s^2}{3}$	–	$\frac{c_s^2}{24}$

The collision matrix is fully determined by the choice of its non-zero eigenvalues and the corresponding eigenvectors. To satisfy the linear stability conditions [32], the non-zero eigenvalues must lie in the interval $]-2, 0[$. Mass vector $\mathbf{1}$ and the vectors $\mathbf{C}_\alpha$ are the eigenvectors associated with the zero eigenvalues — they are the conserved modes in the model. Let $\{\mathbf{e}_k\}$, $k = 0, ..., b_m$ denote the orthonormal basis in momentum space, constructed as the polynomials of the vectors $\mathbf{C}_\alpha$. Let us assume that this basis represents the set of the eigenvectors of the matrix A, associated with the eigenvalues $\{\lambda_k\}$. Following [38], we rewrite Eq. (1a) as its

projection on this basis

$$\tilde{N}_i(\boldsymbol{r},t) = N_i(\boldsymbol{r},t) + \sum_{k=0}^{b_m} \lambda_k (\mathbf{N} - \mathbf{N}^{\mathrm{eq.}}, \mathbf{e}_k) e_{ki} + t_p^\star(\boldsymbol{C}_i, \boldsymbol{F}) \,, \tag{5}$$

$$N_i(\boldsymbol{r} + \boldsymbol{C}_i, t+1) = \tilde{N}_i(\boldsymbol{r},t) \,, \qquad i \in \{0, \ldots, b_m\} \,. \tag{6}$$

Note that Eq. (5) replaces the explicit use of the collision matrix A. The eigenvalues can also be easily adjusted during computations, if necessary, provided that they satisfy the stability constraints. When all non-zero eigenvalues $\{\lambda_k\}$ are set to be equal to $-1/\tau$, equation (5) reduces to the lattice BGK model [7, 67]:

$$N_i(\boldsymbol{r} + \boldsymbol{C}_i, t+1) = N_i(\boldsymbol{r},t) - \frac{1}{\tau}(N_i - N_i^{\mathrm{eq.}}) + t_p^\star(\boldsymbol{C}_i, \boldsymbol{F}) \,. \tag{7}$$

In the case of the lattice BGK equation (7), ρ and $\boldsymbol{J}$ are conserved provided that the equilibrium function satisfies the following conditions

$$(\mathbf{N} - \mathbf{N}^{\mathrm{eq.}}, \mathbf{1}) = 0 \,, \; (\mathbf{N} - \mathbf{N}^{\mathrm{eq.}}, \mathbf{C}_\alpha) = 0 \,, \; \forall \alpha = 1, ..., D \,. \tag{8}$$

The labeling of the discrete velocity sets for $D2Q9$ and $D3Q15$ models in this paper, their basis vectors and associated eigenvectors are given in Section A.1 and Section A.2, respectively.

2.2. Hydrodynamics Equations

The solution for the population function N_i is usually obtained in a perturbative form of Chapman-Enskog expansion [13] in the powers of small perturbation parameter $\epsilon = \delta_x / L$ (L is the characteristic length):

$$N_i(\boldsymbol{r},t) = N_i^{\mathrm{eq.}}(\boldsymbol{r},t) + \epsilon N_i^{(1)}(\boldsymbol{r},t) + \epsilon^2 N_i^{(2)}(\boldsymbol{r},t) + O(\epsilon^3) \,, \; i = 0, ..., b_m \,. \tag{9}$$

The equilibrium population $N_i^{\mathrm{eq.}}(\boldsymbol{r},t)$ can take a form (see [67, 62])

$$N_i^{\mathrm{eq.}} = r_p^\star \rho + t_p^\star \left[J_\alpha C_{i\alpha} + \rho \frac{u_\alpha u_\beta}{2} (3 C_{i\alpha} C_{i\beta} - \delta_{\alpha\beta}) \right] \,, \quad \boldsymbol{u} = \frac{\boldsymbol{j}}{\rho} \,, \; \boldsymbol{J} = \boldsymbol{j} - \frac{1}{2}\boldsymbol{F} \,, \tag{10}$$

Parameter $r_p^\star$ is related with t_p as

$$r_p^\star = t_p^\star c_s^2 \quad \text{when } p \neq 0 \quad \text{and} \qquad r_0^\star = 1 - \sum_{p \neq 0} r_p^\star \,, \tag{11}$$

where c_s is the sound speed of the model, which is to be discussed later. The first order correction to the equilibrium, $N_i^{(1)}$, in standard coordinate system is given in details in Section A.5). One crucial ingredient is that $\epsilon \mathbf{N}^{(1)}$ is isotropic (rotational invariant) and can be written in any orthogonal coordinate system $\{x', y', z'\}$ (z' is omitted in two dimensions) as

$$\epsilon N_i^{(1)} = \frac{1}{\lambda_\psi} \frac{\partial j_{\alpha'}}{\partial \beta'} Q_{i\alpha'\beta'} + \frac{1}{\lambda_e} (\nabla \cdot \boldsymbol{j}) E_i^{\mathrm{im}} \,, \quad \{\alpha', \beta'\} \in \{x', y', z'\} \,, \tag{12}$$

$$\text{where} \quad Q_{i\alpha'\beta'} = t_p^\star \left(C_{i\alpha'} C_{i\beta'} - \frac{c_i^2}{D} \delta_{\alpha'\beta'} \right), \text{ and } \quad E_i^{\mathrm{im}} = t_p^\star \frac{c_i^2}{D} - r_p^\star. \tag{13}$$

Projection of the vectors $\mathbf{N}^{\mathrm{eq.}}$ of equation (10) and $\epsilon\mathbf{N}^{(1)}$ of equation (12) written in the standard coordinate system on the basis vectors $\mathbf{e}_k$ are given by formulas (A.4) and (A.10). The hydrodynamic equations for ρ and $\boldsymbol{j}$ derived from the model are

$$\partial_t \rho + \nabla \cdot \boldsymbol{j} = 0\,, \tag{14a}$$

$$\partial_t \boldsymbol{j} + \nabla \cdot (\frac{\boldsymbol{j} \otimes \boldsymbol{j}}{\rho}) = -c_s^2 \nabla \rho + \nabla \cdot (\nu \nabla \boldsymbol{j}) + \nabla(\nabla \cdot \nu_\xi \boldsymbol{j}) + \boldsymbol{F}\,, \tag{14b}$$

where the kinematic viscosity ν and the bulk viscosity viscosity ν_ξ are related to two non-zero eigenvalues of the collision matrix

$$\nu = \frac{1}{3}(\tau - \frac{1}{2})\,, \qquad \tau \equiv -\frac{1}{\lambda_\psi}\,, \tag{15a}$$

$$\nu_\xi = [\nu(2 - 3\mathcal{C}) + \xi]\,, \qquad \xi = -(\mathcal{C} - c_s^2)(\frac{1}{\lambda_e} + \frac{1}{2})\,, \tag{15b}$$

and for $D2Q9$ and $D3Q15$ models, the coefficient $\mathcal{C}$ is given by

$$\mathcal{C} = \frac{D+2}{3D}\,. \tag{16}$$

For the athermal LBE models, the pressure P is given by the equation of state for an ideal gas,

$$P = c_s^2 \rho\,.$$

By introducing characteristic LB velocity U and assuming the density fluctuates about its average, ρ_0, the pressure can be rescaled in the following dimensionless form:

$$P \to \frac{(P - P_0)}{\rho_0 U^2}\,, \qquad P_0 \equiv c_s^2 \rho_0\,. \tag{17}$$

Using the following scalings

$$x \to x/L\,, \quad t \to tU/L\,, \quad \boldsymbol{u} \to \boldsymbol{u}/U\,, \tag{18}$$

we can write the hydrodynamic equations in the following dimensionless form

$$\mathrm{M}^2 \partial_t P + \nabla \cdot \rho \boldsymbol{u} = 0\,, \tag{19a}$$

$$\partial_t \rho \boldsymbol{u} + \nabla \cdot (\rho \boldsymbol{u} \otimes \boldsymbol{u}) = -\rho_0 \nabla P + \frac{1}{\mathrm{Re}} \nabla \cdot (\nabla(\rho \boldsymbol{u})) + \nabla(\frac{\nu_\xi}{UL} \nabla \cdot (\rho \boldsymbol{u})) + \rho_0 \frac{\vec{1}_g}{\mathrm{Fr}}\,, \tag{19b}$$

where the Reynolds number Re, the Froude number Fr and the Mach number M are defined as the following

$$\mathrm{Re} = \frac{LU}{\nu}\,, \quad \mathrm{Fr} = \frac{U^2}{FL}\,, \quad \mathrm{M} = \frac{U}{c_s}\,. \tag{20}$$

Accordingly, the density can also be written in terms of the dimensionless pressure:

$$\rho = \rho_0 \left(1 + \mathrm{M}^2 P\right). \tag{21}$$

If we choose to neglect the density fluctuation, which is second order in the Mach number M, as indicated in equation (21), we obtain the incompressible Navier-Stokes equations

$$\nabla \cdot \boldsymbol{u} = 0\,, \tag{22a}$$

$$\partial_t \boldsymbol{u} + \boldsymbol{u} \cdot \nabla\, \boldsymbol{u} + \nabla P = \frac{1}{\mathrm{Re}} \nabla^2 \boldsymbol{u} + \frac{\vec{1}_g}{\mathrm{Fr}}\,. \tag{22b}$$

In particular, Stokes equation can be obtained by omitting the nonlinear term in the equilibrium population of equation (10). The sound speed is a free parameter in the equilibrium. The restriction $c_s^2 < \mathcal{C}$ comes from the condition $\xi > 0$ (see equation (15b)). Based on linear stability analysis, the choice of $c_s^2 = 1/3$ is the optimal choice (see [51]) and it also corresponds to the LB models derived by another approaches (cf. [30, 43]). Small Mach number M means that $U << c_s$.

2.3. Interface boundary conditions

In absence of surface tension between two fluids, one heavy and one light, the balance of momentum at the interface according to the Navier-Stokes equation (14b) leads to the following equation at the interface

$$[2\nu \mathsf{Dj} \cdot \boldsymbol{n} - P\boldsymbol{n}]_S = 0\,, \quad \mathsf{Dj} = \frac{1}{2}(\partial_\alpha j_\beta + \partial_\beta j_\alpha)\,. \tag{23}$$

If the density ratio among the two fluids is so disparate so that the dynamic viscosity of the light fluid (*e.g.*, gas) is negligible, the above equation (23) reduces to the following free interface conditions for the heavy fluid (*e.g.*, liquid)

$$P - 2\nu \frac{\partial j_n}{\partial n} = P_0\,, \tag{24a}$$

$$\frac{\partial j_\tau}{\partial n} + \frac{\partial j_n}{\partial \tau} = 0\,,\ \tau \in \{\tau_1, \tau_2\}. \tag{24b}$$

Here j_n and $j_\tau = \{j_{\tau_1}, j_{\tau_2}\}$ are the normal and tangential momentum components of the viscous (heavy) fluid; and P and P_0 are the pressures of the heavy and the light fluids at the interface S, respectively.

3. LATTICE BOLTZMANN MODEL FOR FREE INTERFACE

The populations $\{N_i(\boldsymbol{r}, t)\}$ and the total mass of one fluid $\rho_f(\boldsymbol{r}, t)$ represent the main independent variables of the LB free-surface algorithm. In empty cells, $\rho_f = 0$; in the cells fully filled with fluid, $m_f = \rho$ and in partially filled cells, $0 < \rho_f < \rho$. The collision step is performed only in the "active" cells where $\rho_f \neq 0$. Similar to the VOF method, gravitation force is computed in proportion to current occupation of the cell:

$$\boldsymbol{F} = \frac{\rho_f}{\rho}\left(\rho_0 \boldsymbol{g}\right). \tag{25}$$

The unknown populations at nodes adjacent to interface, which cannot be determined from the lattice Boltzmann equation, are constructed by using Chapman-Enskog analysis up to the first order in the expansion in ϵ.

3.1. First order expansion of N_i at interface

Here we write $\mathbf{N}^{(1)}$ given by the relation (12) in the interface coordinate system $\{x', y', z'\} = (n, \tau_1, \tau_2)$, such that

$$\epsilon N_i^{(1)} = \frac{1}{\lambda_\psi}(\frac{\partial j_\tau}{\partial n} + \frac{\partial j_n}{\partial \tau})Q_{in\tau} + \frac{1}{\lambda_\psi}(\frac{\partial j_n}{\partial n}Q_{inn} + \frac{\partial j_\tau}{\partial \tau}Q_{i\tau\tau}) \tag{26}$$

$$+\frac{\nabla \cdot \boldsymbol{j}}{\lambda_e}E_i^{\mathrm{im}} \ , \ \tau \in \{\tau_1, \tau_2\} \ . \tag{27}$$

In the above equation, the non-diagonal components of the strain-rate tensor Dj are in the prefactor of $\mathbf{Q}_{n\tau}$. From the boundary condition (24b), the terms involving $\mathbf{Q}_{n\tau}$ should be set to zero at the interface. By substitution of the divergence condition $\frac{\partial j_\tau}{\partial \tau} = \nabla \cdot \boldsymbol{j} - \frac{\partial j_n}{\partial n}$, and $Q_{i\tau\tau} = -Q_{inn}$, we obtain the first order solution of N_i at the interface

$$N_i = N_i^{\mathrm{eq.}} + \frac{2}{\lambda_\psi}\frac{\partial j_n}{\partial n}Q_{inn} + \nabla \cdot \boldsymbol{j}\left(\frac{1}{\lambda_e}E_i^{\mathrm{im}} - \frac{1}{\lambda_\psi}Q_{inn}\right) + O(\epsilon^2) \ , \tag{28}$$

in two dimensions. In three dimensions, we first write

$$\frac{\partial j_{\tau_1}}{\partial \tau_1}Q_{i\tau_1\tau_1} + \frac{\partial j_{\tau_2}}{\partial \tau_2}Q_{i\tau_2\tau_2} = \frac{1}{2}\left(\frac{\partial j_{\tau_1}}{\partial \tau_1} - \frac{\partial j_{\tau_2}}{\partial \tau_2}\right)(Q_{i\tau_1\tau_1} - Q_{i\tau_2\tau_2})$$

$$+\frac{1}{2}\left(\frac{\partial j_{\tau_1}}{\partial \tau_1} + \frac{\partial j_{\tau_2}}{\partial \tau_2}\right)(Q_{i\tau_1\tau_1} + Q_{i\tau_2\tau_2}) \ . \tag{29}$$

Then using the divergence condition

$$\frac{\partial j_{\tau_1}}{\partial \tau_1} + \frac{\partial j_{\tau_2}}{\partial \tau_2} = \nabla \cdot \boldsymbol{j} - \frac{\partial j_n}{\partial n} \ ,$$

and the $Q_{i\tau_1\tau_1} + Q_{i\tau_2\tau_2} = -Q_{inn}$, we obtain

$$N_i = N_i^{\mathrm{eq.}} + \frac{3}{2\lambda_\psi}\frac{\partial j_n}{\partial n}Q_{inn} + \frac{1}{2\lambda_\psi}\left(\frac{\partial j_{\tau_1}}{\partial \tau_1} - \frac{\partial j_{\tau_2}}{\partial \tau_2}\right)(Q_{i\tau_1\tau_1} - Q_{i\tau_2\tau_2})$$

$$+\frac{1}{\lambda_\psi}\left(\frac{\partial j_{\tau_1}}{\partial \tau_2} + \frac{\partial j_{\tau_2}}{\partial \tau_1}\right)Q_{i\tau_1\tau_2} + \nabla \cdot \boldsymbol{j}\left(\frac{1}{\lambda_e}E_i^{\mathrm{im}} - \frac{1}{2\lambda_\psi}Q_{inn}\right) + O(\epsilon^2) \tag{30}$$

in three dimensions. Since $\nabla \cdot \boldsymbol{j}$ is of order $O(\mathrm{M}^2)$, it can be neglected in the above equations for incompressible flows. Then using equation (24a) for $\frac{\partial j_n}{\partial n}$, the equations (28) and (30) become

$$N_i = N_i^{\mathrm{eq.}} + \frac{(P - P_0)}{\nu\,\lambda_\psi}Q_{inn} + O(\epsilon^2) \ , \tag{31}$$

in two-dimensions, and

$$N_i = N_i^{\mathrm{eq.}} + \frac{3(P-P_0)}{4\lambda_\psi \nu} Q_{inn} + \frac{1}{2\lambda_\psi}(Q_{i\tau_1\tau_1} - Q_{i\tau_2\tau_2}) \left(\frac{\partial j_{\tau_1}}{\partial \tau_1} - \frac{\partial j_{\tau_2}}{\partial \tau_2} \right) + \frac{1}{\lambda_\psi} Q_{i\tau_1\tau_2} \left(\frac{\partial j_{\tau_1}}{\partial \tau_2} + \frac{\partial j_{\tau_2}}{\partial \tau_1} \right) + O(\epsilon^2) \ , \tag{32}$$

in three dimensions.

The values of the known populations, which propagate from the neighboring active points to the front nodes, are used to compute unknown macroscopic quantities (ρ, $\boldsymbol{j}$, and the derivatives of $\boldsymbol{j}$ tangential to interface) from the above equations by solving the linearized system by means of least square fitting. We refer to local computing of unknown populations at front nodes as *reconstruction step* which is further discussed in Section 3.3.

3.2. Recoloring step

In order to describe two phase behavior, ILB models [27] include two type (color) populations: $\{R_i(\boldsymbol{r},t)\}$ and $\{B_i(\boldsymbol{r},t)\}$. Indeed, ILB operates only on their sums: $\sum_{i=0}^{b_m} R_i(\boldsymbol{r},t)$ and $\sum_{i=0}^{b_m} B_i(\boldsymbol{r},t)$. We represent then the ILB model in an equivalent form [23], by using only populations $N_i(\boldsymbol{r},t)$ and the total mass of the fluid $\rho_f(\boldsymbol{r},t)$ (or mass fraction of one fluid $m_f = \rho_f(\boldsymbol{r},t)/\rho$) as independent variables. Here, $N_i(\boldsymbol{r},t)$ can be interpreted as a sum of $R_i(\boldsymbol{r},t)$ and $B_i(\boldsymbol{r},t)$. Local quantity of the another fluid is equal to $\rho(\boldsymbol{r},t) - \rho_f(\boldsymbol{r},t)$. Recoloring algorithm is employed to advect the quantity ρ_f between the cells by keeping a sharp front. The operation tends to send as much as possible fluid phase into direction of its bulk. For this purpose, one has to find the solution, denoted $\mathbf{R}^{\mathrm{R}}(\boldsymbol{r},t)$, which maximizes the post-collision color flux $\tilde{F}[\mathbf{R}]$ along the normal $\boldsymbol{n}$ to the interface, with

$$\tilde{F}(\mathbf{R}) = \sum_{i=0}^{b_m} R_i \, \boldsymbol{C}_i \cdot \boldsymbol{n} \ , \quad \sum_{i=0}^{b_m} R_i = \rho_f(\boldsymbol{r},t) \ , \quad 0 \le R_i \le \tilde{N}_i(\boldsymbol{r},t) \ . \tag{33}$$

The solution is constrained by mass conservation. Note that, due to the above inequality, this solution exists only when the post-collision populations are positive. Also it is on common unproven belief that this also is required for stability. Below, we call "good" cells where the post-collision populations $\tilde{N}_i(\boldsymbol{r},t)$ in Eq. (5) are positive. The way we treat other cells is described in Section (3.3). In a simplest way, one can find the solution to (33) as follows. Starting from the population whose velocity is the closest to the normal direction (has maximal $(\boldsymbol{C}_i \cdot \boldsymbol{n})$ value)), one goes down to those which has the minimal value and put R_i equal to the maximal possible value ($R_i \le \tilde{N}_i$). The procedure stops when no more color is available ($\sum_{i=0}^{b_m} R_i = \rho_f$). Additional efforts can be required to keep the symmetry of the solution. The new value $\rho_f(\boldsymbol{r},t+1)$ is equal to the sum of all incoming fluid quantities $R_i^{\mathrm{R}}(\boldsymbol{r} - \boldsymbol{C}_i, t)$:

$$\rho_f(\boldsymbol{r},t+1) = \sum_{i=0}^{b_m} R_i^{\mathrm{R}}(\boldsymbol{r} - \boldsymbol{C}_i, t) \ . \tag{34}$$

Since $\rho_f(\boldsymbol{r},t+1)$ can be updated immediately after recolouring steps in neighbouring nodes, no additional storage is needed for the solution $\mathbf{R}^{\mathrm{R}}(\boldsymbol{r},t)$ and this algorithm

reduces the ILB memory requirement by almost a factor two. We compute $\boldsymbol{n}$ similar as in VOF methods [52, 68, 84]

$$\boldsymbol{n} \approx \nabla m_f \ , \tag{35}$$

with the following central difference approximation

$$\boldsymbol{n} = \sum_{i=1}^{b_m} s_i \boldsymbol{C}_i m_f(\boldsymbol{r} + \boldsymbol{C}_i) \ . \tag{36}$$

where

$$s = \begin{cases} 1/4 \times \{2,2,2,2,1,1,1,1\} \ , & \text{for } D2Q9 \ , \\ 1/8 \times \{4,4,4,4,1,1,1,1,1,1,1,1\} \ , & \text{for } D3Q15 \ . \end{cases}$$

Following [63, 68], the method for normal estimation which reproduces a line (a plane) exactly regardless its orientation with respect to fixed coordinate system is referred to as second order method. With this criterion, approximation (36) which is done separately for each cell is only first order accurate. This is confirmed by simple advection tests in Section 7.1. The possibility to have wetting/non-wetting condition at solid boundary is controlled by the following assignment: $\rho_f(\boldsymbol{r}^{solid}) = \rho_f \times w$, $w \geq 0$ in wetting case and $w \leq 0$, otherwise. In computations below we assume mostly that interface is perpendicular to solid boundary: $(\boldsymbol{n}, \boldsymbol{n}^s) = 0$. Here and below, $(n^s, \tau_1^s, \tau_2^s)$ denote the normal and the tangential vector components with respect to the solid wall. In order to model this condition with the relation (36), we define $\rho_f(\boldsymbol{r}^{solid})$ at smooth enough walls as

$$\begin{aligned} &\rho_f(\boldsymbol{r} + \boldsymbol{C}_j) = \rho_f(\boldsymbol{r} + \boldsymbol{C}_i) \ , \\ &\text{if } \boldsymbol{r} + \boldsymbol{C}_j = \boldsymbol{r}^{solid} \ , \ C_{j\,n^s} = -C_{i\,n^s} \ , \text{ and } C_{j\,\tau^s} = C_{i\,\tau^s} \ . \end{aligned} \tag{37}$$

Indeed, the condition (37) uses the same pairs of populations as a specular reflection (55) sketched in Fig. 1b.

3.3. Reconstruction step

According to our algorithm, cell is active if its ρ_f value is positive. We define an interface cell as a cell where the populations are separated into two sets: known and unknown. Known populations are those which arrive from already active cells. Unknown populations are those which would arrive from the non-active cells. We distinguish then two types of interface cells: interface (I) cells are those which have been already active at the previous time step; new interface (N) cells are those which have not been active at the previous time step. Let us denote as I^+ (I^-) the set of indices of locally known (unknown) populations N_i^+ (N_i^-, respectively). The numbers s^+ and s^- of known and unknown populations are related by

$$s^+ + s^- = b_m + 1 \ . \tag{38}$$

One can represent the population expansions (31) and (32) as

$$\mathbf{N} = \mathsf{B}\boldsymbol{X} + \boldsymbol{b} \ , \ \boldsymbol{X} = \begin{cases} \{\rho, j_x, j_y\} \ , \ 2D \ ; \\ \{\rho, j_x, j_y, j_z, \frac{\partial j_{\tau_1}}{\partial \tau_1} - \frac{\partial j_{\tau_2}}{\partial \tau_2}, \frac{\partial j_{\tau_1}}{\partial \tau_2} + \frac{\partial j_{\tau_2}}{\partial \tau_1}\} \ , \ 3D \ . \end{cases} \tag{39}$$

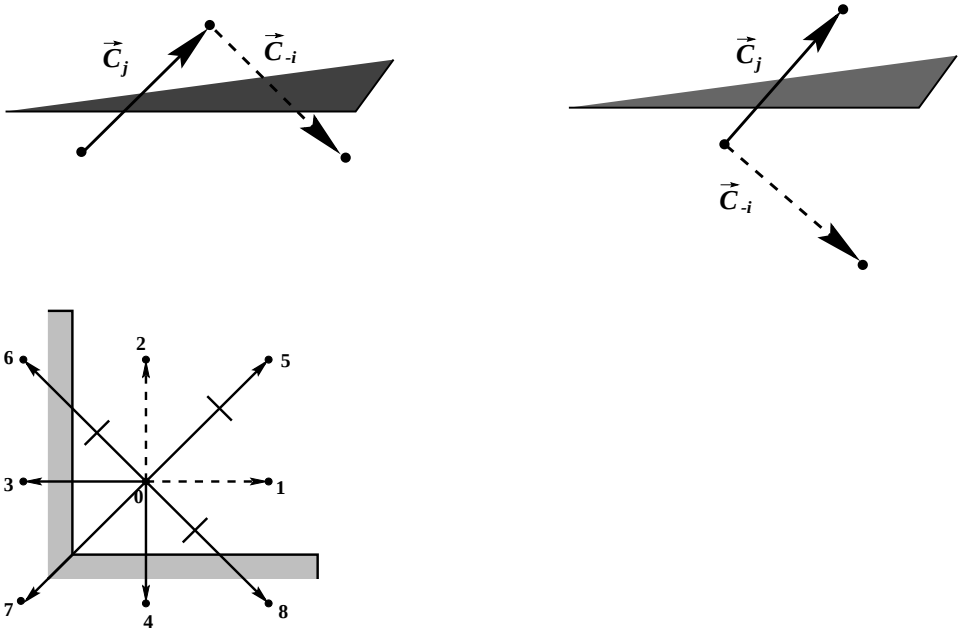

FIG. 1. Left to right: non-local specular reflection, local specular reflexion, 2D corner. In last case, in 2D: $N_1 = \tilde{N}_3$, $N_2 = \tilde{N}_4$, $N_5 = \frac{1}{2}(\tilde{N}_6 + \tilde{N}_8)$, $N_6 = \frac{1}{2}(\tilde{N}_6 + \tilde{N}_7)$, $N_8 = \frac{1}{2}(\tilde{N}_8 + \tilde{N}_7)$.

Vector $\boldsymbol{X}$ contains $n_v = 3$ unknown macroscopic quantities in $2D$ and $n_v = 6$ unknowns in $3D$. When we do not neglect the term $\nabla \cdot \boldsymbol{j}$ in Eqs. (28) and (30), we include it into the list of variables $\boldsymbol{X}$. The elements of the matrix B depend upon the linearization of the equilibrium (10).

Linearization with respect to momentum approximates the nonlinear terms $\rho u_\alpha u_\beta$ in (10) as

$$\rho u_\alpha u_\beta = j_\alpha u_\beta{}^\star \ . \tag{40}$$

Approximate velocity ($u_\beta{}^\star$) and density ($\rho^\star$) values are discussed below. Let us introduce $Q_{i\alpha}$:

$$Q_{i\alpha} = \sum_\beta \frac{u_\beta{}^\star}{2}(3C_{i\alpha}C_{i\beta} - \delta_{\alpha\beta}) \ , \ \forall \alpha = 1, ..., D \ . \tag{41}$$

Then for the $D2Q9$ model the coefficients in (39) are

$$B_{i,1} = r_p^\star + \frac{c_s^2}{\nu}\frac{1}{\lambda_\psi}Q_{inn} \ , \tag{42a}$$

$$B_{i,2} = t_p^\star(C_{ix} + Q_{ix}) \ , \tag{42b}$$

$$B_{i,3} = t_p^\star(C_{iy} + Q_{iy}) \ , \tag{42c}$$

$$b_i = -\frac{1}{\nu}\frac{1}{\lambda_\psi}P_0 Q_{inn} - \frac{1}{2}t_p^\star\frac{\rho_f}{\rho^\star}\rho_0(\boldsymbol{C}_i, \boldsymbol{g}) \ . \tag{42d}$$

and for the $D3Q15$ model:

$$B_{i,1} = r_p^\star + \frac{3c_s^2}{4\nu}\frac{1}{\lambda_\psi}Q_{inn} \ , \tag{43a}$$

$$B_{i,2} = t_p^\star(C_{ix} + Q_{ix}) \ , \tag{43b}$$

$$B_{i,3} = t_p^\star(C_{iy} + Q_{iy}) \ , \tag{43c}$$

$$B_{i,4} = t_p^\star(C_{iz} + Q_{iz}) \ , \tag{43d}$$

$$B_{i,5} = Q_{i\tau_1\tau_1} - Q_{i\tau_2\tau_2} \ , \tag{43e}$$

$$B_{i,6} = Q_{i\tau_1\tau_2} \ , \tag{43f}$$

$$b_i = -\frac{3}{4\nu}\frac{1}{\lambda_\psi}P_0 Q_{inn} - \frac{1}{2}t_p^\star\frac{\rho_f}{\rho^\star}\rho_0(\boldsymbol{C}_i, \boldsymbol{g}) \ . \tag{43g}$$

Approximation to force-term (25) appears in $\boldsymbol{b}$ since we consider here $\boldsymbol{j}$ and not $\boldsymbol{J}$ as an unknown variable in $\boldsymbol{X}$ (cf. (10)). The linearized equations to find $\boldsymbol{X}$ correspond to S^+ known populations N_i^+:

$$B_{ij}X_j = r_i \ , \ r_i = N_i^+ - b_i \ , \ i \in I^+ \ . \tag{44}$$

One can introduce further constraints on $\boldsymbol{X}$. We considerably improve stability and accuracy when the solution is required to fulfill approximate density definition (3a) in a form:

$$\rho - \sum_{i\in I^-} N_i^- = \sum_{i\in I^+} N_i^+ \ . \tag{45}$$

Substitution of the population expansion (39) into (45) for N_i^- yields an additional equation:

$$\sum_j B_{\rho,j}X_j = r_\rho \ , \tag{46a}$$

$$B_{\rho,1} = 1 - \sum_{i\in I^-} B_{i,1} \ , \tag{46b}$$

$$B_{\rho,k} = -\sum_{i\in I^-} B_{i,k} \ , \ , k = 1, ..., n_v \tag{46c}$$

$$r_\rho = \sum_{i\in I^+} N_i^+ + \sum_{i\in I^-} b_i \ . \tag{46d}$$

This completes assembling of the matrix B and the vector $\boldsymbol{b}$. Different from the relation (40) linearizations of the equilibrium can be proposed.
Linearization with respect to density, in particular, treats the non-linear term as

$$\rho u_\alpha u_\beta = \rho u_\alpha{}^\star u_\beta{}^\star \ . \tag{47}$$

In case (47), one can take $\boldsymbol{J}$ itself as a component in $\boldsymbol{X}$. This avoids approximation of the density (cf. (42a)- (43a)). In 2D, for example, relations (42a) are modified

as follows:

$$B_{i,1} = r_p^\star + \frac{c_s^2}{\nu}\frac{1}{\lambda_\psi}Q_{inn} + t_p^\star \sum_{\alpha\beta}\frac{u_\alpha{}^\star u_\beta{}^\star}{2}(3C_{i\alpha}C_{i\beta} - \delta_{\alpha\beta}) \ , \tag{48a}$$

$$B_{i,2} = t_p^\star C_{ix} \ , \tag{48b}$$

$$B_{i,3} = t_p^\star C_{iy} \ , \tag{48c}$$

$$b_i = -\frac{1}{\nu}\frac{1}{\lambda_\psi}P_0 Q_{inn} \ , \tag{48d}$$

$$\boldsymbol{X} = \{\rho, J_x, J_y\} \ . \tag{48e}$$

Linearized system of equations (44), (45) contains $m = s^+ + 1$ equations: $2 \le m \le b_m + 1$. The number of variables n_v is equal to the number of components of the vector $\boldsymbol{X}$. When $n_v \le m$, we solve the linear system by using fast least-square method with permutations. Single Value Decomposition Method [66] can be used as well but it has been found to be much slower for linear systems used here. If the linear solver detects that the system is singular, or when $n_v > m$, we use extrapolations for unknown populations from neighbor "good" active points (as defined in Section 3.2). Similar procedure is employed when appear negative populations after the reconstruction or after collision. We show below that the relative part of "bad" situations is very small in stable calculations. When combinations of tangential derivatives in 3D are not included to $\boldsymbol{X}$ (39), one does not need then to construct tangential vectors $\boldsymbol{\tau}_1$ and $\boldsymbol{\tau}_2$. Moreover, this reduces the number of singular cases since the number of unknowns decreases from $n_v = 6$ to $n_v = 4$. No important impact on the solution was detected because of this approximation.

Approximate values $\rho^\star$ and $\boldsymbol{u}^\star$ are obtained as follows. In already active I-cells, the previous time step solution is used. In new interface N-cells, an extrapolation from the active cells lying as close as possible along the normal $\boldsymbol{n}$ is employed. At least one neighbor active node always exists by the definition of N-cell, otherwise it would not be activated. Since the collision, and hence update of ρ and $\boldsymbol{u}$, is done first in B- and I- cells, reconstruction step in N-cells can use current solutions in neighbor "good" nodes for extrapolations (see the steps **6**, **7**, **8** of the algorithm below). Additionally, other successful N-cells can be used for extrapolations.

The summary of the local reconstruction procedure reads:

1. Compute $\boldsymbol{n}$. When necessary, compute $\boldsymbol{\tau}_1$ and $\boldsymbol{\tau}_2$.
2. Extrapolate (in time or space) velocity and density values.
3. Compute B and $\boldsymbol{b}$.
4. Solve linearized system.
5. Compute unknown populations in a form (39).

One can then iterate the steps $\mathbf{3} - \mathbf{5}$ by using velocity/density values obtained at a previous sub-iteration for approximations. We detect, however, only weak influence of this procedure on the accuracy/stability.

3.4. Brief Outline of the Numerical Algorithm

We initialize first ρ_f in all liquid cells at $t = 0$. The populations are then initialized to their equilibrium values, and first collision step is performed in active cells where $\rho_f > 0$. We refer to active cells as $A(t)-$cells below. Subsequent steps at time t, $t = 0, ..,$ are:

1. Compute $\rho_f(\boldsymbol{r}, t+1)$ in all cells by recoloring technique.
2. Divide all cells into active/non-active cells:
$(\boldsymbol{r}, t+1) \in A(t+1)$ if $\rho_f(\boldsymbol{r}, t+1) > 0$; otherwise it is non-active.
3. Propagate populations from $A(t)$ into $A(t+1)$ cells.
4. Classify known/unknown populations in $A(t+1)$ cells: $N_i(\boldsymbol{r}, t+1)$ is marked as *known population* if $(\boldsymbol{r} - \boldsymbol{C}_i, t) \in A(t)$. Otherwise it is marked as *unknown population.*
5. Divide $A(t+1)$ cells into B/I/N-cells:

   - $(\boldsymbol{r}, t+1)$ is marked as B(*bulk*)-cell if it has obtained only known populations.
   - $(\boldsymbol{r}, t+1)$ is marked as I(*interface*)-cell if it has obtained at least one unknown population and if $(\boldsymbol{r}, t) \in A(t)$.
   - $(\boldsymbol{r}, t+1)$ is marked as N(*new interface*)-cell if $(\boldsymbol{r}, t) \notin A(t)$.

6. Perform collision in B-cells.
7. Perform reconstruction and collision in I-cells.
8. Perform reconstruction and collision in N-cells.
9. $t = t + 1$; Go to **1**.

This completes the short description of the LB free interface algorithm.

4. BOUNDARY CONDITIONS

4.1. No-slip boundary conditions

While applying the method in very complex geometries, we currently accept its "step-wise" cell-centered discretization on the regular rectangular grids. We apply at boundary nodes the bounce-back rule (b.b.) where the populations leaving the fluid return to the node of departure with the opposite velocity:

$$N_{-i}(\boldsymbol{r}, t+1) = \tilde{N}_i(\boldsymbol{r}, t) \,, \qquad \text{if} \quad \boldsymbol{r} + \boldsymbol{C}_i \in \text{solid} \,, \quad \boldsymbol{C}_{-i} = -\boldsymbol{C}_i \,. \tag{49}$$

Let us first consider the condition (49) at order $O(\epsilon^0)$, *i.e.* when

$$N^{\text{eq.}}_{-i}(\boldsymbol{r}, t) = N^{\text{eq.}}_i(\boldsymbol{r}, t) \,. \tag{50}$$

and therefore, momentum projection on the link $\boldsymbol{C}_i$ should vanish at $\boldsymbol{r}$:

$$(\boldsymbol{j} \cdot \boldsymbol{C}_i)(\boldsymbol{r}, t) = 0 \,. \tag{51}$$

Substitution of the first order expansion (12) written along a link $\boldsymbol{C}_i$ into the b.b condition (49) holds

$$[(\boldsymbol{j} \cdot \boldsymbol{C}_i) + \Delta \times \nabla(\boldsymbol{j} \cdot \boldsymbol{C}_i)\boldsymbol{C}_i](\boldsymbol{r}, t) = 0 + O(\epsilon^2) + O(M^2) + ... \,, \; \Delta = \frac{1}{2} \,. \tag{52}$$

Closure relation (52) locates the walls in the middle between the current node $\boldsymbol{r}$ and the neighbor node $\boldsymbol{r}+\boldsymbol{C}_i$. So, at order $O(\epsilon^1)$:

$$(\boldsymbol{j}\cdot\boldsymbol{C}_i)(\boldsymbol{r}+\frac{1}{2}\boldsymbol{C}_i,t)=0\,. \tag{53}$$

Condition (53) is exact for linear flow only, similar as its generalizations [12, 59], which annihilate $(\boldsymbol{j}\cdot\boldsymbol{C}_i)$ at a given distance $\Delta\boldsymbol{C}_i$ between $\boldsymbol{r}$ and $\boldsymbol{r}+\boldsymbol{C}_i$. When second order Chapman-Enskog expansion is substituted into b.b. condition, *i.e.* the second order momentum derivatives are taken into account, the analysis [17, 20, 39] shows that effective wall location depends on the choice of the whole set of the eigenvalues. So far, it depends on the kinematic and bulk viscosities values. It depends also upon wall inclination with respect to the lattice. Modification of momentum definition by $\frac{1}{2}\boldsymbol{F}$ [cf. Eqs. (3b) and (10)] enables us to analyze obtained closure relations independently on the force term in Eq. (5) since b.b holds:

$$-\frac{1}{2}t_p^\star(\boldsymbol{C}_i,\boldsymbol{F})\overbrace{+}^{\text{force}}t_p^\star(\boldsymbol{C}_i,\boldsymbol{F})=\frac{1}{2}t_p^\star(\boldsymbol{C}_i,\boldsymbol{F})=-\frac{1}{2}t_p^\star(\boldsymbol{C}_{-i},\boldsymbol{F})\,. \tag{54}$$

In general flows, effective precision of the b.b. rule is something between first and second order. It is only first order accurate, however, in inclined channels as shown in [19]. In order to improve the precision of the b.b. boundary conditions, we apply *magic solution* for eigenvalues (A.13)-(A.15a). This solution fulfills exactly closure relation (53) for Poiseuille flow for channels parallel to x, y or z lattice axis. Relation (A.13) represents a particular case of the solution [39], since here all eigenvalues associated with the even (odd) order polynomial basis vectors are set equal between them. The solution (A.13) provides viscosity-independent wall location for Stokes flow in any geometry. When $\lambda_\psi\to-2$, the first order collision (A.16) is not as precise as the magic collision for b.b rule but is still acceptable, since in the limit $\nu\to 0$, the influence of second order terms on the effective wall position goes to zero.

4.2. Free-slip boundary condition

Free-slip boundary condition has not been so intensively studied as the bounce-back condition for the LB models. Following Maxwell [5, 57], specular reflections are used in the LB methods to model it: when the population arrives on the solid from a boundary node, it reflects into the node symmetric with the respect to the normal to the wall (see Fig. 1a). Using first order Chapman-Enskog expansion [6, 11, 26], one can show that *specular* reflection at a solid wall provides *free slip boundary condition*

$$j_{n^s}=0\,;\quad \frac{\partial j_{\tau^s}}{\partial n^s}+\frac{\partial j_{n^s}}{\partial\tau^s}=0\,,\quad \tau^s=\{\tau_1^s,\tau_2^s\}\,. \tag{55}$$

Formally, condition (55) holds up to $O(\epsilon^2)$ only when the flow is invariant along a wall. In general then, *local* specular reflection (see Fig. 1b) has approximately the

same accuracy. We implement it in a form:

$$N_{-i}(\boldsymbol{r}, t+1) = \tilde{N}_j(\boldsymbol{r}, t) \ , \quad \text{if} \quad \{\boldsymbol{r}+\boldsymbol{C}_i, \boldsymbol{r}+\boldsymbol{C}_j\} \in \text{solid}$$
$$\text{and} \quad C_{-in^s} = -C_{jn^s} \ , \quad C_{-i\tau^s} = C_{j\tau^s} \ . \tag{56}$$

Relations (55) mean that all populations return into the node of departure. Unlike to bounce-back, force addition in (5) is not consistent with the condition (55) when $\boldsymbol{F}$ is parallel to the wall. To improve this, one should either omit the corresponding force addition to leaving populations $\tilde{N}_j(\boldsymbol{r}, t)$, or to implement specular reflection in its classical *non-local* form, when the populations are reflected into the neighboring nodes. In geometries more complicated than the point near a solid wall, the solution for an unknown population should involve more than one post-collision population. For instance, in the case of "2D" corner (see in Fig. 1c), we compute unknown "corner" populations, both in $2D$ and in $3D$, as an arithmetical mean of specular reflections with respect to both walls forming the angle. This provides free-slip condition (55) approximately on the both sides. Useful test of free-slip boundary conditions is a uniform Stokes flow in an infinite (periodic) channel. This solution is maintained exactly by the relations (55) in 2D case and by using mentioned above reflections in corners, in 3D case. Similar, free interface algorithm should provide exact solution with density and velocity equal to those at the inlet when constant flux comes into a channel. Linear combination of free-slip/no-slip boundary conditions with some factor $p/(1-p)$ enables us to model intermediate friction behavior.

4.3. Inlet boundary condition

Inlet boundary condition is not trivial even in the case of a constant incompressible flux $\boldsymbol{j}^{in} = \rho_0 \boldsymbol{U}^{in}$ entering the domain. Indeed, the density $\rho^{in}(\boldsymbol{r}, t)$ at the inlet is not equal to its initial value ρ_0 because of the pressure gradients. So far, $\rho^{in}(\boldsymbol{r}, t)$ is *a priori* unknown. Moreover, since mass flux $\boldsymbol{j}$ performs the ρ_f-transport for the recoloring algorithm, $\boldsymbol{j}$ should be proportional to the effective ρ^{in} value and therefore can not be set equal to $\boldsymbol{j}^{in}$. In order to compute ρ^{in}, we use the same idea as for the reconstruction step: all populations are expressed as a first order Chapman-Enskog expansion where the velocity is set equal to its inlet value. Known populations, arriving at the inlet from the bulk, are used to derive the unknown quantities. In particular, when the velocity derivatives at inlet are negligible (e.g., constant profile) and continuity condition (19a) is assumed, $\epsilon N_i^{(1)}$ (12) written in non-inclined coordinate system becomes becomes:

$$\epsilon N_i^{(1)} = \frac{1}{\lambda_\psi} \frac{\partial \rho}{\partial \beta} U_\alpha^{in} Q_{i\alpha\beta} \ , \quad i \in \{0, \ldots, b_m\} \ . \tag{57}$$

Assuming an approximately hydrostatic (linear) pressure distribution at inlet $c_s^2 \partial\rho/\partial z \approx \rho_0 g$, the populations take the form

$$N_i = \rho B_i + b_i \ , \tag{58}$$

where

$$B_i = r_p^\star + t_p^\star \left[U_\alpha^{in} C_{i\alpha} + \frac{U_\alpha^{in} U_\beta^{in}}{2} (3C_{i\alpha}C_{i\beta} - \delta_{\alpha\beta}) \right] \ , \ b_i = \frac{\rho_0 g}{c_s^2} \frac{1}{\lambda_\psi} U_\alpha^{in} Q_{i\alpha z} - \frac{1}{2} \rho_0 g C_{iz} \ .$$

Computing a sum of known populations $\sum_{i \in I^+} N_i^+$, we write then equation (45) for density:

$$\rho = \frac{\sum_{i \in I^+} N_i^+ + \sum_{i \in I^-} b_i}{1 - \sum_{i \in I^-} B_i} \ . \tag{59}$$

When ρ is computed, incoming populations are imposed in the form (58). In case of not uniform inlet profile, the same approach has to include the first and, if necessary, second order momentum derivatives into Chapman-Enskog expansion for inlet populations.

5. OVERVIEW OF THE ALGORITHM

We apply our method to simulate filling processes. The scaling procedure is based on the equality of the Reynolds number Re and Froude number Fr to those of the experiment (see (20)). The magnitude of the inlet LB velocity U^{lb}, $U^{lb} = \| \boldsymbol{U}^{in} \|$, determines the scaling factor between the LB and the physical velocities. Characteristic length L is set equal to some inlet distance. Consider some regular grid which covers the computational domain. Let the number of its liquid cells be equal to V and their number at inlet be S^{in}. The number of LB time steps to fill the box is $T^{lb} = V/(S^{in} U^{lb})$. Since the computational time is the inverse of proportional to U^{lb}, its value must be as high as possible. On the other side, the conditions $U^{lb} < 1$ and $U^{lb} < c_s$ should be met. Moreover, $\mathrm{M}^2 = {U^{lb}}^2 / c_s^2$ should be small enough to avoid high compressibility error. For instance, in case when nearly hydrostatic regime $\nabla P' \approx \mathrm{Fr}^{-1}$ is attained in a box of a height H, the density difference $\rho - \rho_0$ between the top and the bottom is about $[\rho_0 / c_s^2] g^{lb} H$. When the physical velocity increases in l times but the same inlet velocity is used in different LB simulations, g^{lb} and density variation decreases as l^2. So far, simulations corresponding to high physical velocities are easier for the method from the point of view of the compressibility effects caused by the gravitation.

In simulations below, we mostly use $U^{lb} \leq 0.1$ and $c_s^2 = 1/3$, *i.e.* $\mathrm{M}^2 \leq 0.03$ at inlet, at least. According to von Neumann analysis of the linearized stability [51, 77, 83], the minimal stable viscosity value ν^{min} increases with U^{lb}. When $U^{lb} = 0.1$, the LB method without free interface approaches its stability boundary somewhere at $\tau^{min.} \approx 0.5078$ in 32^2 and 64^2 periodic boxes. This data corresponds to first order collision (A.16) according to our stability analysis. In case of simulations with free interface and $U^{lb} \approx 0.1$, we detect a loss of stability at approximately this range of τ values, *i.e.* at moderate Reynolds numbers ($\mathrm{Re} \approx 200 - 500$ for typical inlet length $L^{lb} \approx 10 l.u$). The development of instabilities manifests itself, for example, in appearance of a large number of negative populations after the reconstruction. In fact, local velocities overhead the inlet velocity several times in real-life simulations. The non-linearity of the flow (see [83]) and the presence of free boundary can shift the stability bounds to greater viscosity values as well.

When the grid is refined by a factor p, *i.e.* $V \to p^3 V$, $S \to p^2 S$, and U^{lb} is reduced by a factor k, $k \geq 1$, T^{lb} increases as $p \times k$ times and the total computational efforts increase accordingly by a factor about $p^3 \times p \times k$. Since Mach number decreases as k^2, one should not expect decreasing of the compressibility effects when $k = 1$ even if the grid is refined. The stability should improve, however, since ν^{lb} increases by a factor p/k. In reality, ν^{lb} should take so small values for high Reynolds number simulations that it appears to be un-practical to improve the stability only with a help of the refining procedure. In order to analyze the problem, two approaches have been investigated. The first one is to study different reconstruction strategies, including higher order extrapolations, iteratively improved linearizations, explicit/implicit time approximations, etc. In spite of some improvement, no important gain in stability has been obtained unless some numerical diffusion is introduced into the scheme. This represents our second approach to stabilize the LB method as discussed in the next section.

6. UPWIND APPROACHES

So far three possibilities have been explored in [22]. As a first (*explicit upwind*) approach we add numerical diffusion explicitly as shown below. In the next approach, in order to reduce crosswind diffusion of such an explicit upwind scheme in multi-dimensions, we represent the equilibrium function of the LB equation in such a form that derived macroscopic equations may include different corrections to diffusion tensor. In this way, we introduce LB analogs of full upwind scheme and different streamline type upwind schemes. As a last possibility to damp the small-scale fluctuations, the simplest turbulent (Smagorinsky) model was considered similar to [37]: $\nu \to \nu + \nu_T, \nu_T = C_s^2 ||\mathsf{D}||$. The intrinsic locality of the LB method is maintained in almost all new schemes since all components of strain-rate tensor $\mathsf{Dj} = \rho \mathsf{D}$ are derived from non-equilibrium part of the population solution. When a spectrum of global evolution operator is improved for the first and third approaches, the LB method becomes robust and stable. *Explicit upwind scheme* has been found to be the most robust for free interface simulations. Robustness means here that very different realistic problems can be modeled using nearly equal upwind parameters without loss of stability.

The idea of Pe-dependent numerical diffusion borrowed from the framework of the conventional approaches in case of 1D convection-diffusion problem (see [9]):

$$\nu \frac{\partial^2 \phi}{\partial y'^2} - UH \frac{\partial \phi}{\partial y'} = 0 \ , \ U > 0 \ , \ 0 \leq y' = y/H \leq 1 \ , \ \phi(0) = 1 \ , \ \phi(1) = 0. \qquad (60)$$

The exact solution is

$$\phi(y') = \frac{e^{ky'} - e^k}{1 - e^k} \ , \quad k = \frac{UH}{\nu} \ . \qquad (61)$$

Exact LBE solution to Eq.(60) is discussed in [29]:

$$\phi(y' = jh) = \frac{\chi^j - \chi^n}{1 - \chi^n} \ , \ \chi = \frac{1 + \mathrm{Pe}}{1 - \mathrm{Pe}} \ , \ \mathrm{Pe} = \frac{Uh}{2\nu} \ , \ h = \frac{H}{n} \ , \ j = 0, ..., n \ . \qquad (62)$$

This solution will coincide with the solution (61) if

$$\chi^n = \exp^k \ , \text{ i.e } \mathrm{Pe}(\nu^{eff}) = \frac{\exp^{k/n}-1}{\exp^{k/n}+1} \ , \text{ i.e } \nu^{eff} = \frac{Uh}{2}\frac{\exp^{k/n}+1}{\exp^{k/n}-1} \ . \qquad (63)$$

Relation (63) means that the effective LB viscosity should be changed ($\nu \to \nu^{eff}$) to obtain exact solution for linear convection-diffusion problem. In other words, high order terms in this flow population solution add the negative diffusion to the viscosity coefficient ν, computed from the first order Chapman-Enskog expansion. In order to compensate it, one can introduce artificial numerical diffusion ν^{num}:

$$\begin{aligned} \nu^{num} &= \nu^{eff} - \nu \\ &= \nu \times \mathrm{Pe}(\frac{\exp^{2\mathrm{Pe}}+1}{\exp^{2\mathrm{Pe}}-1} - \frac{1}{\mathrm{Pe}}) \\ &= \nu \times \mathrm{Pe} \times f(\mathrm{Pe}) \ , \ f(\mathrm{Pe}) = \coth(\mathrm{Pe}) - \frac{1}{\mathrm{Pe}} \ , \ \mathrm{Pe} = \frac{k}{2n}. \end{aligned} \qquad (64)$$

Relation (63) means that when exactly the same quantity of the numerical diffusion ("optimal rule") as for finite difference methods [9] is added, LB solution to the problem (60) becomes exact.

With the "explicit upwind approach", we adjust locally λ_ψ so that ν becomes equal to ν^{eff}:

$$\nu^{eff} = \nu + \nu^{num} \ , \ \nu^{num} = \nu \times F(\mathrm{Pe}) \ , \ F(\mathrm{Pe}) = C \times \mathrm{Pe} \times f(\mathrm{Pe}) \ , \ \mathrm{Pe} = \frac{\parallel u \parallel h}{2\nu} \qquad (65)$$

Here, the local Peclet number Pe (or grid Reynolds number) controls the quantity of the numerical diffusion; $\parallel u \parallel$ is magnitude of local velocity; space step h is equal to 1 l.u; C is some free parameter. In order to reduce ν^{num} at least at small and intermediate Pe numbers, we introduce *modified critical approximation* (cf. [3]):

$$f(\mathrm{Pe}) = 0 \ , \ \mathrm{Pe} < \mathrm{Pe}^{crit.}, \text{ and } f(\mathrm{Pe}) = (1 - \frac{\mathrm{Pe}^{crit.}}{\mathrm{Pe}}) \ , \ \mathrm{Pe} > \mathrm{Pe}^{crit.} \ . \qquad (66)$$

We assume here, that an estimation obtained from the stability analysis for maximal stable Peclet number Pe^{max} enables us to fix $Pe^{crit.}$ value, $Pe^{crit.} \leq Pe^{max}$. Let $\nu^{crit.}(\parallel u \parallel)$ corresponds locally to $Pe^{crit.}$: $\nu^{crit.} = \parallel u \parallel h/2Pe^{crit.}$. Then we can rewrite relations (65), (66) as

$$\begin{aligned} \nu^{num}(\nu) &= 0 \ , \ \nu^{eff}(\nu) = \nu \ , \text{ if } \nu > \nu^{crit.} \ , \\ \nu^{num}(\nu) &= (\nu^{crit.} - \nu)[C \times Pe^{crit.}] \ , \text{ and} \\ \nu^{eff}(\nu) &= [C \times Pe^{crit.}]\nu^{crit.} + [1 - C \times Pe^{crit.}]\nu \ , \text{ if } \nu < \nu^{crit.} \ . \end{aligned} \qquad (67)$$

Relations (67) mean that the numerical diffusion manifests itself only when the kinematic viscosity is less than critical viscosity value at a given velocity. Effective viscosity (67) is represented as a linear combination of $\nu^{crit.}$ and ν. Its magnitude depends on a product of two values: $Pe^{crit.}$ and C. When $C \times Pe^{crit.} = 1$, ν^{eff} takes its minimal value $\nu^{crit.}(\nu)$. We study results obtained with a help of explicit

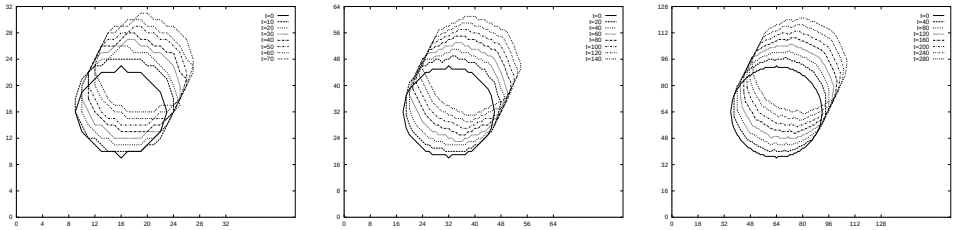

FIG. 2. Advection of 2D bubble with $\boldsymbol{U} = (0.05, 0.1)$. Top to bottom: 32^2, 64^2, and 128^2 grids.

upwind scheme in case of one phase examples (1D convection-diffusion, driven cavity) and benchmark free interface simulations (see in [22]). Based on these results, we conjecture that the choice $Pe^{crit.} = D$ and $C = 1/D$ is close to limit of the admissible numerical diffusion on fine enough grids. In this way, ν^{eff} approaches critical approximation [3] to solution [9] in 1D case. Note that in case $U^{lb} = 0.1$, choice $Pe^{crit.} = 3$ corresponds to $\tau = 0.55 \gg \tau_{min}$. The assumption that the LB stability limits can be estimated in terms of Pe number is currently under study.

7. NUMERICAL RESULTS

7.1. Advection tests.

As a simple advection test of the recoloring algorithm, we advance a bubble with a given constant velocity $\boldsymbol{U}$ by using free interface LB method for grids with different resolution. Figure 2 demonstrates that the bubble shape is maintained. Initially, the active points are those lying inside the bubble ($\rho_f = \rho_0$). In all active points, the population solution stays equal to Stokes equilibrium $N_i^{\mathrm{eq.}}(\rho_0, \boldsymbol{U})$ after each propagation step. Consequently, the density ρ and velocity $\boldsymbol{u}$ stay equal to their initial values ρ_0 and $\boldsymbol{U}$. For the convergence study, regular grids $(2^n)^D$, $n \geq n_0$ are used. Space step is set equal to 1 l.u. for every grid. The initial radius of bubble is $7 \times 2^{(n-n_0)}$ l.u., $n_0 = 5$ and its initial position is $\boldsymbol{r}_0 = (2^{n-1})^D$. The position of bubble center $\mathbf{R}(t)$ is approximated as ρ_f/ρ-weighted sum of the active cells centers. The error err in bubble center position is computed as the arithmetical mean of its coordinate values:

$$err = \frac{2^{n_0-n}}{D} \sum_{\alpha=1,\ldots,D} \sum_{t} \parallel (R_\alpha(t) - R_\alpha^{\mathrm{e}\cdot}(t)) \parallel , \ \mathbf{R}^{\mathrm{e}\cdot}(t) = \mathbf{R}_0 + \boldsymbol{u}t \ . \qquad (68)$$

Error is measured in discrete time moments $t = \{10 \times k \times 2^{(n-n_0)}\}$, $k = 1, ..., 7$. The norm of the difference $rel(n) = \sqrt{\frac{err(n)}{err(n+1)}}$ is computed for each pair of the consequently refined grids. Linear (quadratic) convergence should correspond to $rel(n) = \sqrt{2}$ ($rel(n) = 2$), respectively. Results obtained in case of different advection velocities and $D3Q15$ model are found in Tables 2 and 3. Convergence rates between first and second order are agree with the prediction of Section 3.2. As it could be expected, the error is anisotropic. Similar results are obtained for other $\boldsymbol{U}$ values and for $D2Q9$ model. More complicated advection tests defined by Rider & Kothe [68] are in study [46].

7.2. Filling in 2D cavity

TABLE 2
Error norm in 3D for bubble advection in case (36).

velocity $\boldsymbol{U}$	32^3	64^3	128^3
$\boldsymbol{U} = (0.1, 0, 0)$	0.2464	0.0603	0.0168
$\boldsymbol{U} = (0.1, 0.1, 0.1)$	0.2011	0.0696	0.0321
$\boldsymbol{U} = (0.05, 0.1, 0)$	0.2489	0.1031	0.0301
$\boldsymbol{U} = (0.05, 0.1, 0.05)$	0.2727	0.0923	0.0271

TABLE 3
Convergence results for data in Table 2.

velocity $\boldsymbol{U}$	$32-64$	$64-128$
$\boldsymbol{U} = (0.1, 0, 0)$	2.0216	1.8953
$\boldsymbol{U} = (0.1, 0.1, 0.1)$	1.7001	1.4733
$\boldsymbol{U} = (0.05, 0.1, 0)$	1.5537	1.8509
$\boldsymbol{U} = (0.05, 0.1, 0.05)$	1.7186	1.8443

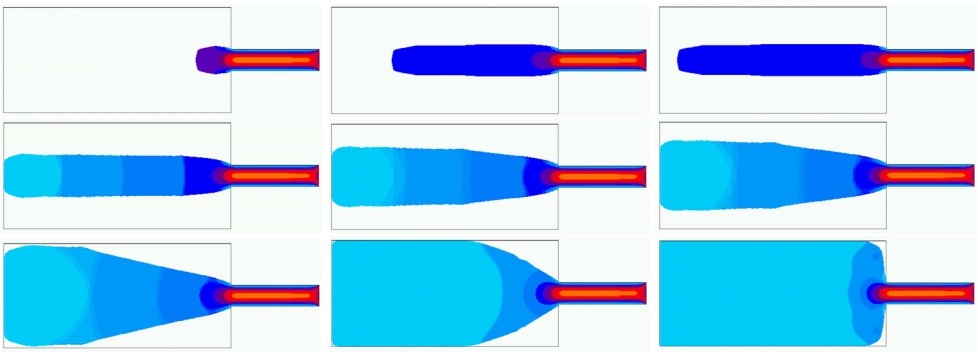

FIG. 3. LB simulation of filling of a 2D cavity at Re = 0.2. The figure shows the time-evolution of the velocity magnitude distribution in the cavity (left to right then top to bottom, $t = 0.11$ s, 0.27 s, 0.32 s, 0.43 s, 0.54 s, 0.59 s, 0.75 s, 0.92 s, and 1.02 s). Physical parameters are: $U = 100$ cm/s, $\nu^{exp} = 1.0$ cm^2/s, $T = 1.08$ s, and $L^{exp.} = 2$ cm. The number of cells is 86,240. The parameters used in the simulation are: $U^{lb} = 0.00625$, $\nu^{lb} = 1.25$, $\tau = 4.25$, $L^{lb} = 40$, and $T^{lb} = 344,960$. No-slip boundary conditions are applied at walls, and the magic collision of Eq. (A.13) is also used. Colors: yellow ($214 - -232$ cm/s), red ($125 - -143$ cm/s), and blue (< 71 cm/s).

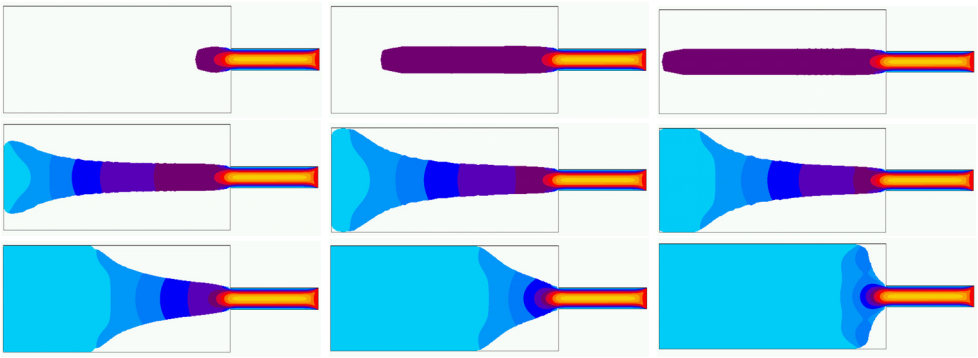

FIG. 4. LB simulation of filling of a 2D cavity at Re = 2. The viscosity is $\nu^{exp} = 0.1$ cm^2/s ($\tau = 0.875$). Other parameters and conditions remain the same as in Fig. 3. Colors: yellow ($157 - -171$ cm/s), red ($100 - -114$ cm/s), and blue (< 43 cm/s).

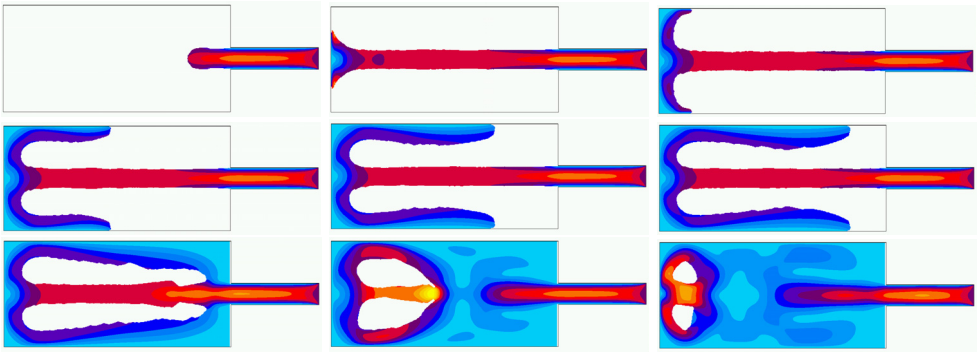

FIG. 5. LB simulation of filling of a 2D cavity at Re = 50. The viscosity is $\nu^{exp} = 0.04$ cm^2/s ($\tau = 0.74$), $U^{lb} = 0.1$ and $T^{lb} = 21,560$. First order collision (A.16) is used. Other parameters and conditions remain the same as in Fig. 4. Colors: yellow ($196 - -232$ cm/s), red ($125 - -143$ cm/s), and blue (< 71 cm/s).

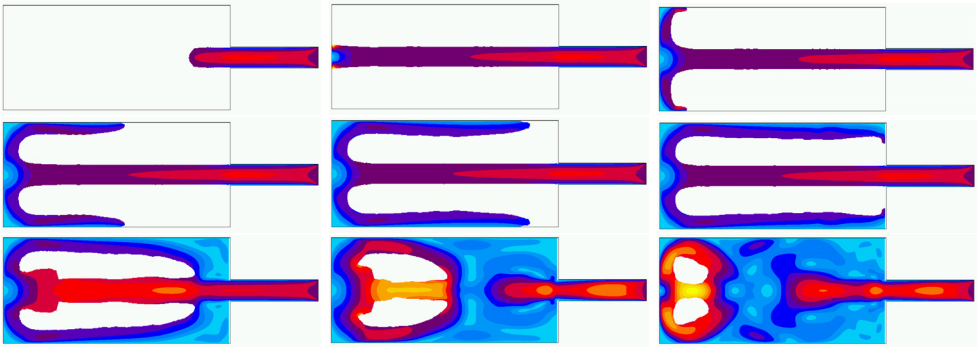

FIG. 6. LB simulation of filling of a 2D cavity at Re = 500. The viscosity is $\nu^{exp} = 0.004$ cm^2/s ($\tau = 0.524$). Friction factor p is set to 1/2. Other parameters and conditions remain the same as in Fig. 5. Colors: yellow ($196 - -232$ cm/s), red ($125 - -143$ cm/s), and blue (< 71 cm/s).

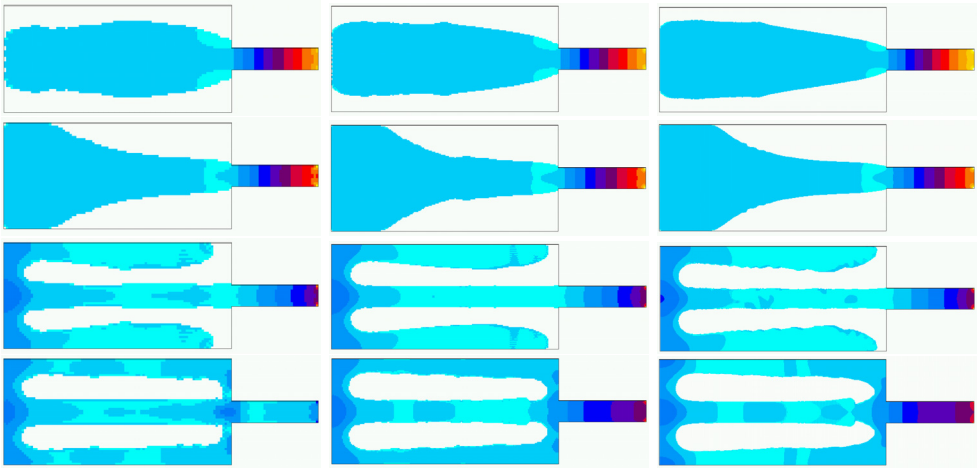

FIG. 7. Pressure solutions in 2D cavity at $t = 0.65$ s with different space resolutions (left to right, space step is: $h = 0.2cm$; $h = 0.1cm$; $h = 0.05cm$) and different Re numbers (top to bottom, Re = 0.2, 2, 50, 500). Reference pressure of gas phase at interface is $P_0 = 1013$ mBar. Colors: Re= 0.2, yellow (3622 − −4096 mBar), red (2673 − −2910 mBar), and blue (< 1724 mBar); Re= 2, yellow (1327 − −1356 mBar), red (1213 − −1242 mBar), and blue (< 1099 mBar); Re= 50, yellow (1048 − −1040 mBar), red (1036 − −1033 mBar), and blue (< 1025 mBar); Re= 500, yellow (1078 − −1073 mBar), red (1048 − −1043 mBar), and blue (< 1033 mBar).

We consider first filling simulations in 2D cavity with expansion 1 : 5. Inlet section is 2 cm × 7.8 cm, the cavity is 10 cm × 20 cm; inlet velocity is equal to 100 cm/s, filling time T is 1.08 s. Gravitation is absent: $\boldsymbol{g} = 0$. Density of fluid $\rho^{exp.}$ is 1 g/cm^3. We vary Reynolds number Re with viscosity. No special efforts to maintain the symmetry is done. We show the obtained results in Figs. 3-6 for Re = 0.2, 2, 50, 500, respectively. In whole, filling patterns are in agreement with the theoretical and the numerical analysis [1]. At Re= 0.2, the "mound filling" is observed. At Re= 2, the filling behavior is changed and "disk pattern" develops. Relatively small LB velocities are used in both cases in order to decrease LB viscosities and therefore, to improve an accuracy of boundary conditions.

At intermediate and high Re, when inertia dominates, filling patterns change drastically and so called "shell" type filling is obtained at Re= 50 and Re= 500. At Re=50, viscous boundary layers are rather thick (see in Fig. 5). At Re= 500, the boundary patterns are much thinner and they develop almost parallel to adjacent wall, in according to the analysis of inviscid flow [1]. Similar solution are obtained at Re> 500, when we use explicit upwind scheme (67) with $C = 1$ and $Pe^{crit.} = 1$. When this scheme is applied in case Re= 50, no influence on the solution is detected since the actual Pe-numbers are less than $Pe^{crit.}$. We conclude then that for chosen parameters of the upwind scheme, the quantity of the numerical diffusion is acceptable.

The convergence behavior of the algorithm with respect to the space resolution is checked by considering three consequently refined grids. In so far, the solution above corresponds to finest grid of the sequence. The results are displayed in Fig. 7 for pressure solution. At given Re number, equal inlet LB velocities are used for simulations at every grid. Then the CFL value is constant (CFL= $U^{lb}\Delta t^{lb}/\Delta x^{lb}$, $\Delta t^{lb} = 1$, $\Delta x^{lb} = 1$) and the value of time step in physical units decreases together with the

space step when the grid is refined. Figure 8 displays point-wise difference $L_{h,2h}(t)$ between the solution obtained on the grid with step $2h$ and its projection from the finer grid, measured in L_1 norm: $L_{h,2h}(t) = \| f_h(t) - f_{2h}(t) \|$. Projection is set equal to an arithmetical mean of the four fine cells lying inside one coarse cell. The solution is put equal to zero in non-filled cells. The results are given for pressure(mBar), velocity(cm/s) and phase-distribution variable ρ_f/ρ: $f = \{P, \| u \|, \rho_f/\rho\}$. The last figure in each row plots the error ratio $L_{h,2h}(t)/L_{2h,4h}(t)$ for these variables. The error is measured each 5% of filling. Mean ratio value is about 2 what corresponds to first order convergence. Table 4 displays integrated over the whole period of filling time convergence rates $L_{h,2h} = \sum_t L_{h,2h}(t)$ vers $L_{2h,4h} = \sum_t L_{2h,4h}(t)$.

The results for convergence rates reflect quite well main features of the current algorithm with respect to mesh refinement. First, only first order convergence is observed. In 2D case, since no tangential derivatives are neglected, second order accuracy is met by Chapman-Enskog expansion at interface as well as in bulk. However, we can not expect effective second order behavior from the boundary conditions at solid walls used here. Also, the advection scheme and the calculations of the normal are only first order accurate. Second, the difference between the solutions obtained on three grids is smaller for intermediate Reynolds numbers, Re= 2 and Re= 50. At Re= 0.2, *i.e.* at high τ values ($\tau > 1$), the difference between coarse/fine solutions at the stagnation point is quite significant. We relate this to inaccuracy of the boundary conditions which grows together with ν (see [17, 39]). For Re = 500, if equal parameters of upwind scheme ($Pe^{crit.} = 1$, $C = 1$) are used on every grid, the numerical diffusion on coarse grids becomes excessive. This can be understood from the relation (67): since $Pe^{crit.}$ and U^{lb} values are equal at all grids, $\nu^{crit.}$ values are also close, whereas the imposed viscosity values ν increases with the refinement. This implies higher ν^{num} values for smaller ν values, *i.e.* for coarse grids. One could assume then that the parameter C should be reduced together with ν. The calculations on the bottom of the Fig. 7 are performed with increasing C values ($C = 1/4, 1/2, 1$), from coarser to finest grids. The results improve then according to our predictions (see at the end of the Section 6). We note, however, that some thickening appears when the boundary flux drains into the inlet column (see the bump at the left of the inlet on right bottom picture in the Fig. 7); this thickening continues to travel with the fluid (see the left bottom pictures in Figs. 5 and 6). We conjecture that this is related to coupling of the populations which carry fast and slow momentum values at interface cells. This effect is less visible on coarse grids (see bottom pictures in Fig. 7) due to excessive numerical diffusion and/or lack of space resolution. Similar results are obtained with the SPH approach by J. Kuhnert and S. Tiwari [44]. We suppose that adding surface tension would smooth the solution.

Compressibility study is performed for Re=2 when inlet velocities varies: $U^{lb} = 0.1 \times 2^{-n}$, $n = 0, 1, 2, 3, 4$. In two first cases, *i.e.* at high τ values ($\tau = \{7.5, 3.5\}$), the solution is neither accurate nor stable. In the three other cases, we compute mean density value $\bar{\rho}(t)$ over all active points and compare it with the reference value ρ_0. We plot in Fig. 9a obtained results for $\delta\rho$ value, $\delta\rho = (\bar{\rho} - \rho_0)$. In order to check if $\delta\rho(n)$ scales as ${U^{lb}}^{2n}$, we rescale $\delta\rho$ with respect to its value at $n = 4$. Figure 9b displays δ^s_ρ values, $\delta^s_\rho = (\bar{\rho} - \rho_0) \times 4^{4-n}$. When $n = 4$, $U^{lb} = 0.1/2^4$, $\mathrm{M}^2 \approx 1.2 \times 10^{-4}$, $\delta\rho \approx 0$, *i.e.* incompressible regime is practi-

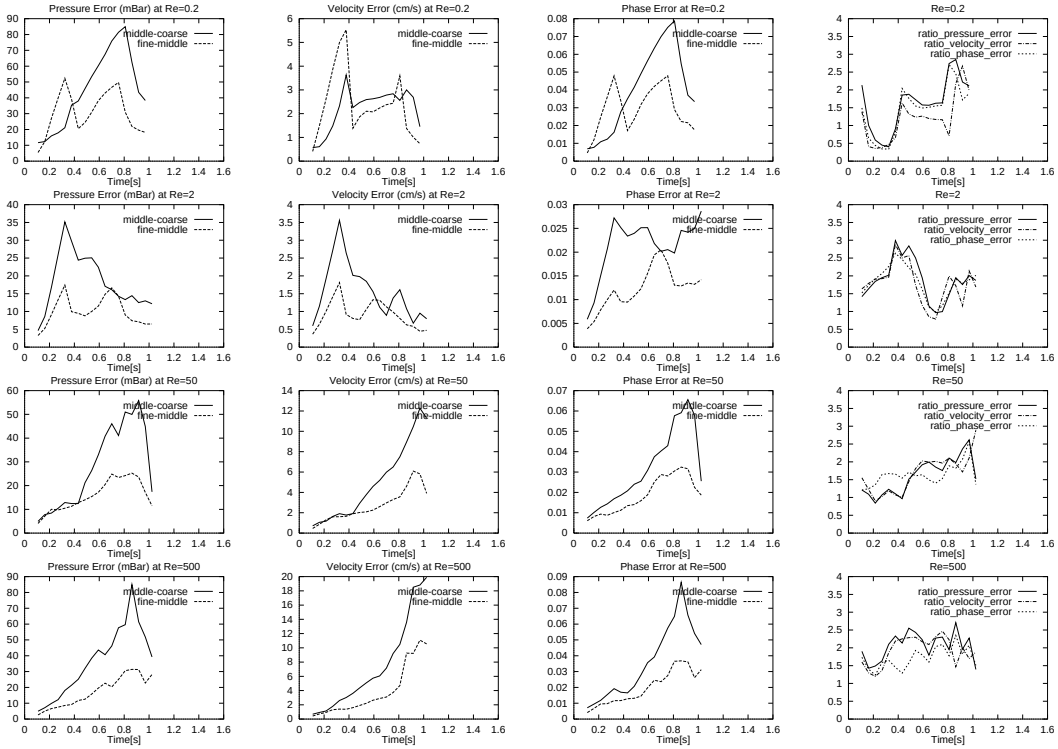

FIG. 8. Left to right, magnitude of error value for pressure, velocity magnitude and fluid quantity ρ_f/ρ between coarse-middle and middle-fine grids in 2D cavity simulations. The last figure in each row plots the error ratio (coarse-middle to middle-fine) for these variables. Top to bottom: Re = 0.2, 2, 50, 500. Data correspond to previous picture.

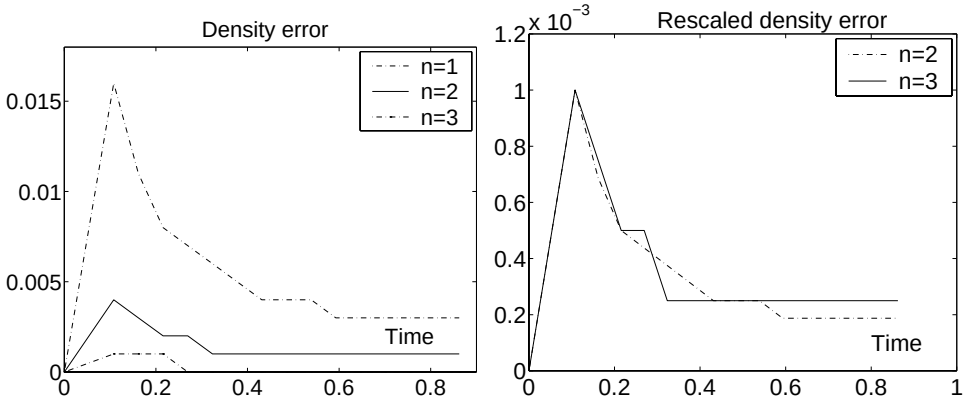

FIG. 9. Density deviations from the reference value at Re = 2, $L^{lb} = 40$. Results are plotted for LB inlet velocities $U^{lb} = 0.1 \times 2^{-n}$, where $n = 2, 3, 4$. Accordingly, $\nu^{lb} = 2 \times 2^{-n}$, $\tau = \{2, 1.25, 0.875\}$. a: $\delta\rho = (\bar{\rho} - \rho_0)$. b: $\delta^s_\rho = (\bar{\rho} - \rho_0) \times 4^{4-n}$.

TABLE 4
Error norm $L_{h,2h}/L_{2h,4h}$ in 2D cavity.

Re	Pressure(mBar)	$\| u \|$ (cm/s)	ρ_f/ρ
0.2	1295.9/553.4	49.44/41.7	0.705/0.51
2.0	330.7/180.4	28.45/16.5	0.39/0.22
50	496.9/282.5	89.6/48.6	0.57/0.33
500	654.68/311.5	144.1/69.09	0.98/0.36

cally reached. After rescaling, density deviations $\delta^s_\rho(n)$ approaches to zero, similar to the results for $n = 4$. This confirms that the compressibility errors scales as M^2, in agreement with the theoretical predictions.

7.3. Three-dimensional simulations.

Benchmark simulations: Hammer box [36] , Campbell box [73] and Sheffield box [2] are presented. The influence of inlet velocity on the compressibility is considered in "Motorblock" simulations. Density of fluid $\rho^{exp.}$ is $1g/cm^3$ unless specially indicated. Since very high Re numbers are modeled, free-slip boundary conditions are mostly used. No-slip boundary conditions correspond to high local velocities in narrow channels and lead to further increase of the compressibility. Filled volume is computed as a sum of vof-type value $m_f = \rho_f/\rho$. The deviation of the obtained filling state in time from the exact linear solution is controlled. In benchmark simulations below, corresponding compressibility error lies within 5%.

Regular computational grids used here include from 10^5 to 2×10^6 liquid cells. Similar results are obtained by using both linearizations discussed in Section 3.3. The code is parallelized using Dynamical Load Balance strategy [45]. Since the non-local operations (compared with one phase LB method) are concentrated at interface cells only (e.g calculation of normal vectors, advection of fluid mass, extrapolations), the method keeps its advantages for parallelization.

Hammer box [36]. We show in Figs. 10 and 11, pressure and velocity fields during mold filling simulations of steel hammer head casting at Re=$53,417$, Fr = 5.1. LB simulations at $U^{lb} = 0.1$ are done with explicit upwind scheme (67), where $Pe^{crit.} = 3$ and $C = 1/3$. The filling sequence agrees quite well with the other results [36, 53]. The stream reaches first the right wall at a the point which lies approximately at a height equal to 2/3 of the distance between the runner and the bottom. The jet of failing steel attains the velocity $250 - 260$ cm/s, then it slows down at the bottom and raises slow into the casting box. During the rise, the pressure reaches the hydrostatic distribution. When the numerical diffusion increases and viscous/gravitation effects prevail over the inertia, the stream comes into the runner and falls down (see in [22]). In so far, this test can be used as a measure of the effective Reynolds numbers. Also, because of very small LB viscosity values used in this experiment, local Pe numbers take mostly high values. Indeed, $Pe^{crit.} = 3$ corresponds to $\| u \| \approx 7 \times 10^{-5}$ in this experiment. One can assume that numerical diffusion can be switched on at higher $Pe^{crit.}$ numbers. For instance,

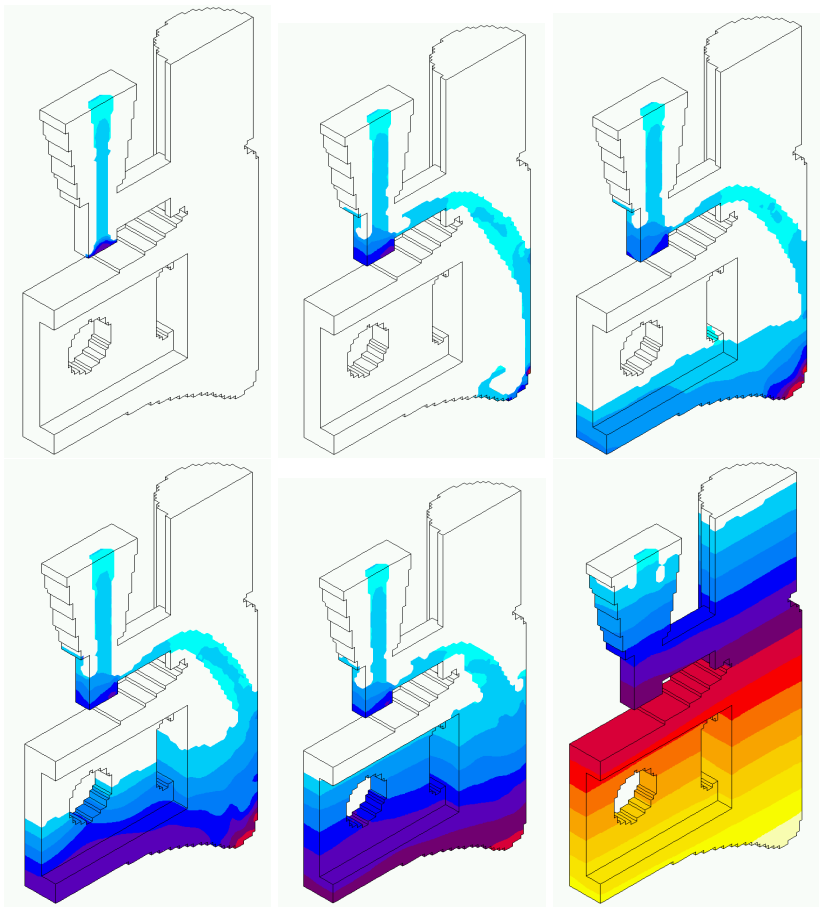

FIG. 10. Filling sequence of pressure distribution in Hammer Box, close to symmetry plane, at Fr = 5.1, Re = 53,417 (left to right and top to bottom, 1.25%, 7.5%, 25%, 35%, 50%, 100% of exact filling). Physical parameters are: $U = 122.859$ cm/s, $\nu^{exp} = 6.9 \times 10^{-7}$ m^2/s, $T = 15$ s, $L^{exp.} = 3$ cm. Grid: 110,573 liquid cells. LB: $U^{lb} = 0.1$, $\nu = 1.1 \times 10^{-5}$, $\tau = 0.500034$, $L^{lb} = 6$, $T^{lb} = 36,858$. Colors: yellow (1339−1366 mBar), red (1203−1230 mBar), and blue(< 1122 mBar).

the results at $Pe^{crit.} = 150$, $C = 1/3$ (*i.e.* $\tau^{crit.}_{\|u\|=0.1} = 0.501$) are still similar to those presented in Figs. 10 and 11. On the other hand, the stabilization is not strong enough when $Pe^{crit.} = 10^3$, *i.e.* $\tau^{crit.}_{\|u\|=0.1} = 0.50015$). This agrees with the stability values mentioned above. The work in progress should help to estimate *a-priori* effective τ and/or Pe stable values in function of other physical parameters.

Analysis of the algorithm is applied to current example. The number of interface points is of order of several thousands at each time step (see Fig. 12a). Figures 12b- 12d display the number of points where at least one unfavorable situation mentioned at caption happens. The number of "bad" cases is negligible compared with the total number of points where the reconstruction takes place. Extrapolations of populations from neighboring "good" cells are performed when situations b), c) or d) happen. Figures 12e–12f display the number of such points. If no such neighbor is found, the point is deactivated. The total number of deactivated nodes over the whole period of filling is equal to six in this example. Due to the stabilizing scheme, no negative population after collision appears. Otherwise

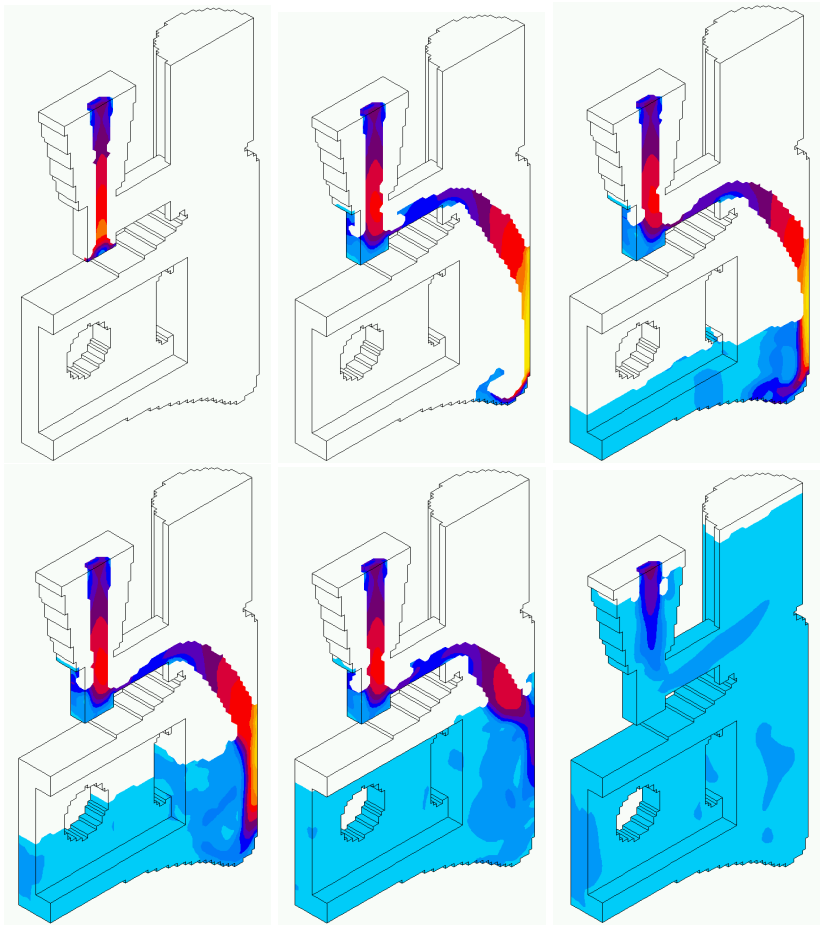

FIG. 11. Filling sequence of the velocity magnitude distribution in Hammer Box. Parameters are the same in Fig. 10. Colors: yellow ($257 - -279$ cm/s), red ($150 - -171$ cm/s), and blue (< 86 cm/s).

the number of negative populations after the reconstruction and after the collision increase drastically when τ approaches its limit value $\tau = 0.5$.

Campbell box [73]. Numerical and experimental results in this geometry (see in Figs. 13 and 14) have been discussed at VII Modeling of Casting and Welding Processes Conference. We model the mold casting by using constant inlet velocity which corresponds approximately to the prescribed filling time. Simulation results at $\mathrm{Re} = 3.2$ are shown in Fig. 13. They agree well with the polymer flow predictions [73]. Filling sequence at $\mathrm{Re} \approx 165$ is plotted in Fig. 14. Here, the sprue develops fast along the bottom of the runner, then impacts to the nearest side of the gate and expands first to the left. Then the sprue fountains quickly to the right. Later, two vortices appear on the either side of the main filling stream. In this way, the simulations reproduce the main features of the experimental results [73]. Note that the kinematic viscosity of the aluminum (and hence Re number) is reduced here, since no turbulent modeling is used in the simulations.

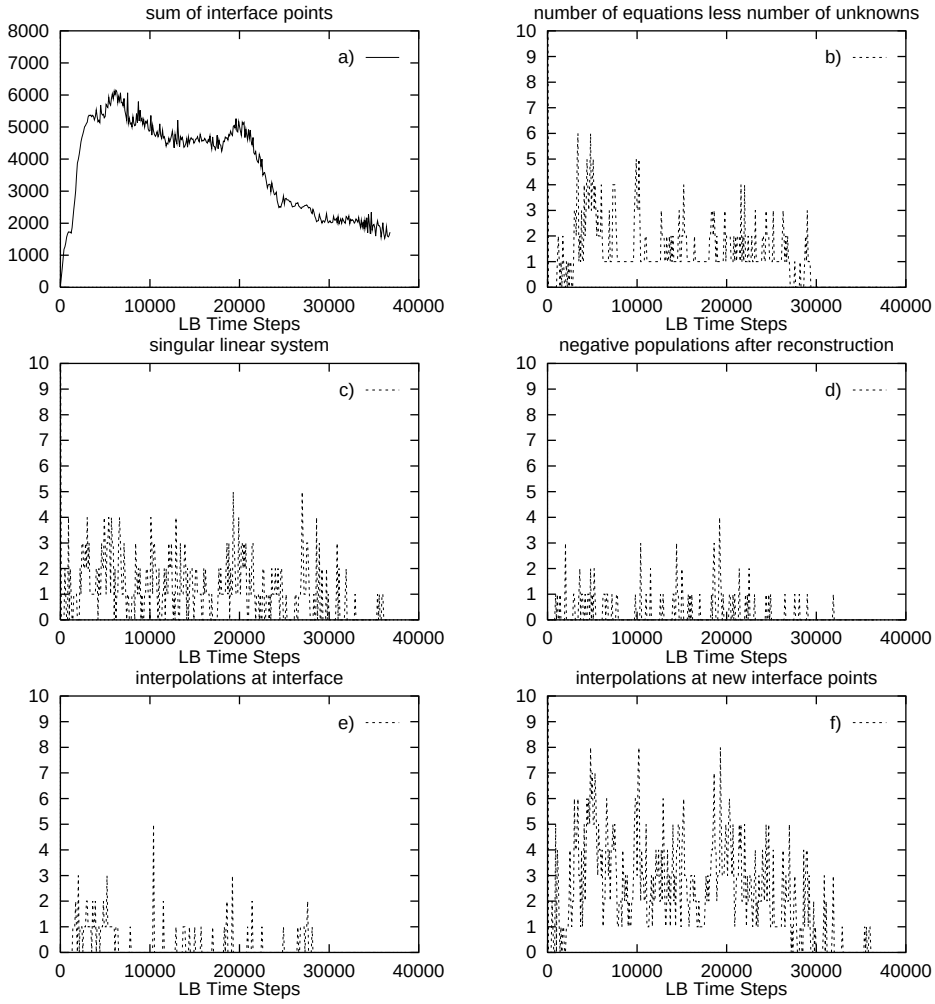

FIG. 12. Analysis of the algorithm for Hammer Box. a: Total number of interface points. b: Number of equations m is less than number of variables n_v. c: $m \geq n_v$ but the linear system is singular. d: Number of cells where negative populations appear after the reconstruction. e: Number of interface cells where interpolations need. f: Number of new interface cells where interpolations need. Here, only interpolations because of b)-d) are accounted.

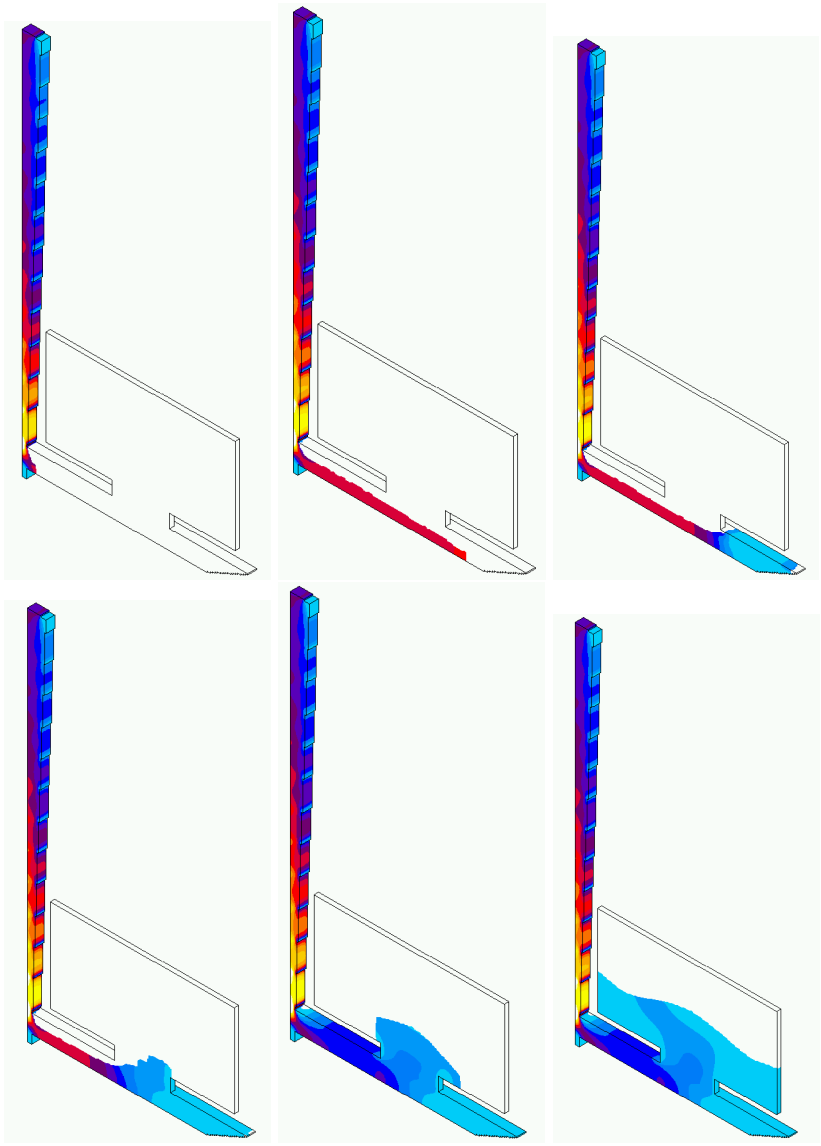

FIG. 13. Velocity magnitude in Campbell Box at Fr = 5.56, Re = 3.2 (left to right and top to bottom, $t = 0.14$ s,0.24 s,0.28 s,0.33 s,0.38 s, 0.47 s.) Physical parameters are: $U = 88.6$ cm/s, $\nu^{exp} = 4 \times 10^{-3}$ m^2/s, $T = 1.88$ s, $L^{exp.} = 1.44$ cm. Grid: 216,546 liquid cells. LB: $U^{lb} = 0.0125$, $\nu^{lb} = 0.047$, $\tau = 0.641$, $L^{lb} = 12$, $T^{lb} = 111,049$. Free-slip boundary conditions. Colors: yellow ($214 - -232$ cm/s), red ($125 - -143$ cm/s), and blue (< 71 cm/s).

Sheffield box [2]. The simulations at Re= 24,717, Fr = 10.7 in Sheffield box are displayed in Fig. 15 in case when $U = 145$ cm/s. They correspond to physical parameters of water. Flow comes from left to right and the variation in inlet velocity results in different values of maximal height of the jet column in the right gate. Our results at inlet velocities $U = 80$ cm/s, 95 cm/s, 105 cm/s, 145 cm/s agree well with the available experimental data [2] and the numerical simulations [53]. For all inlet velocities, we use the same upwind parameters: $Pe^{crit} = 3$, $C = 1/3$. When C increases to 1, however, right water jet does not reach the top wall at

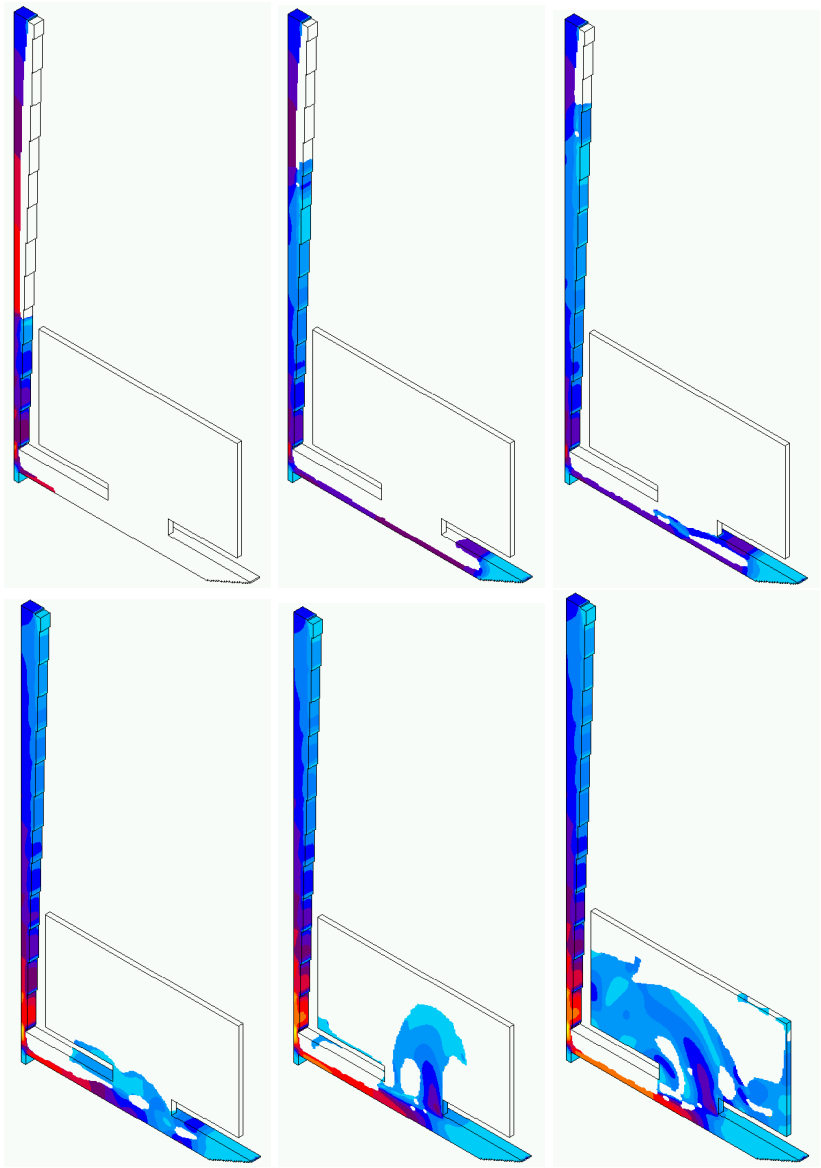

FIG. 14. Velocity magnitude in Campbell Box at Fr = 5.965, Re = 165 (left to right and top to bottom, t = 0.09 s, 0.18 s, 0.227 s, 0.32 s, 0.35 s, 0.45 s). Physical parameters are: $U = 91.75$ cm/s, $\nu^{exp} = 8 \times 10^{-5}$ m^2/s, $T = 1.815$ s, $L^{exp.} = 1.44$ cm. Grid: 216, 546 liquid cells. LB: $U^{lb} = 0.05$, $\nu^{lb} = 0.047$, $\tau = 0.641$, $L^{lb} = 12$, $T^{lb} = 27,762$. Free slip boundary conditions. Colors: yellow ($314 - -371$ cm/s), red ($200 - -229$ cm/s), and blue (< 114 cm/s).

$U = 145$ cm/s, indicating that the gravitation and viscous forces dominate over the convective ones (see in [22]). Similar to the jet behavior in the Hammer box, this test is a good indicator of the excessive numerical diffusion.

Filling sequence in "Motorblock" at Re = 26, 507, Fr = 2.36 is shown in Fig. 16. The results are obtained with strong upwind parameters $Pe^{crit.} = 1$ and $C = 1$. The compressibile effect is much stronger here than for the Hammer and Sheffield boxes when the same inlet velocity ($U^{lb} = 0.1$) is used. It causes, in particular, a quite noticeable delay in filling time. The filling state (in percent of full stand) is

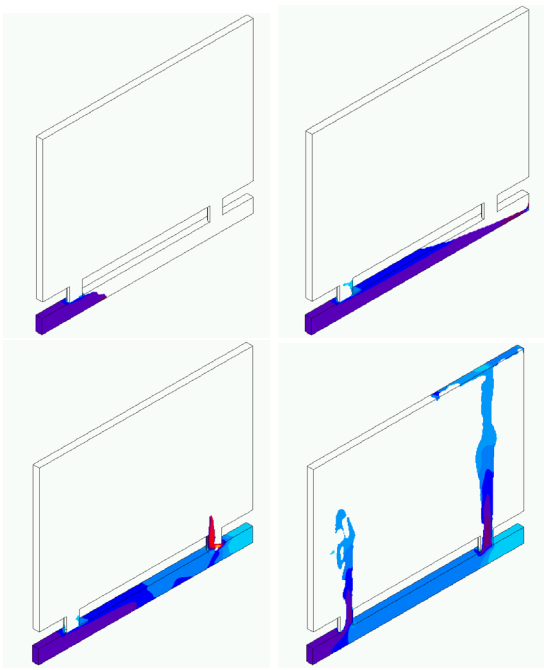

FIG. 15. Velocity magnitude in Sheffield box at Fr = 10.7, Re = 24,717 (left to right and top to bottom, t = 0.06 s, 0.17 s, 0.23 s, 0.4 s). Physical parameters are: U = 145 cm/s, $\nu^{exp} = 1.17 \times 10^{-6}$ m^2 /s, T = 2.31 s, $L^{exp.}$ = 2 cm. Grid: 1,270,420 liquid cells. LB: $U^{lb} = 0.1$, $\nu^{lb} = 8.1 \times 10^{-5}$, $\tau = 0.500243$, $L^{lb} = 20$, $T^{lb} = 33,432$. Free-slip boundary conditions. Colors: yellow (393 − −464 cm/s), red (250 − −286 cm/s),blue (< 143 cm/s).

plotted as a function of time in Fig. 17a for $U^{lb} = 0.1$ and $U^{lb} = 0.025$. Figure 17b displays the error in filling state divided by factor 4 for $U^{lb} = 0.1$. Since both solution are close we can conclude that the error in filling time scales with M rather than with M^2. Note that even for $U^{lb} = 0.025$, the pressure in narrow channels (see inlet channels at two last pictures in Fig. 16, for instance), is still too high. The compressibility of the method is controlled by the choice of the LB characteristic velocity at the inlet: while reducing U^{lb}, pressure solution improves and correct filling time approaches. Nevertheless, an efficient strategy to maintain reasonable Mach numbers in realistic calculations needs still to be found.

8. CONCLUSION

A general approach for free interface Lattice Boltzmann method has been described. This approach is based on a first-order Chapman-Enskog expansion of the population at interface nodes. Boundary conditions at curvilinear interfaces are exactly met by the coefficients of the series. Interface advection is performed with help of locally mass conserving and anti-diffusive recoloring algorithm. Since no stage of the algorithm involves geometrical interface constructions, the method is robust to any interface topology and can be regarded as a surface capturing method. In bulk, second order LB accuracy in space is maintained. At the interface, formal second order accuracy is kept by the expansion. At solid boundaries, actual accuracy of local reflections is something between first and second order. Boundary method [19] can be incorporated for further improvement. Least square minimization pro-

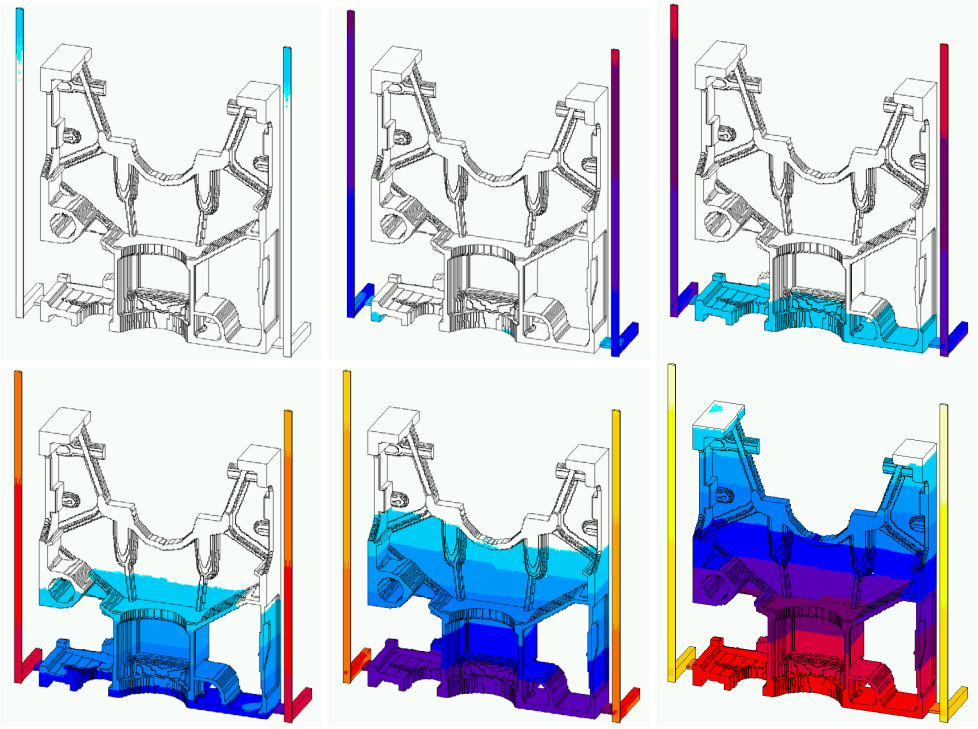

FIG. 16. Pressure distribution is shown at Motorblock at Re $= 26,507$, Fr $= 2.36$ (left to right and top to bottom, $t = 0.3$ s, 2.5 s, 7.52 s, 15 s, 20 s, 25 s; accordingly, 1.25%, 10%, 30%, 60%, 80%, 100%.) Physical parameters are: $U = 83.23$ cm/s, $\nu^{exp} = 9.42 \times 10^{-6}$ m^2 /s, $T = 30.08$ s, $L^{exp.} = 3$ cm, $\rho^{exp.} = 7$ g^3 /cm^3. Grid: 625,817 liquid cells. LB: $U^{lb} = 0.025$, $\nu^{lb} = 6.0 \times 10^{-6}$, $\tau = 0.500017$, $L^{lb} = 6$, $T^{lb} = 200,261$. Free-slip boundary conditions. Colors: yellow ($2181 - -2500$ mBar), red ($1765 - -1863$ mBar), and blue (< 1438 mBar).

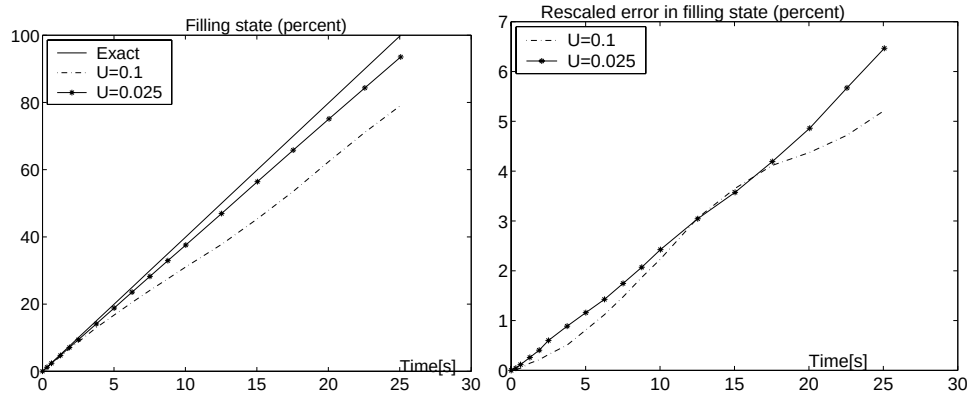

FIG. 17. Comparison of the effective filling of the box with the exact filling in case $U^{lb} = 0.025$ and $U^{lb} = 0.1$. Left: filling state (percents). Right: absolute error is divided by factor 4 in case $U^{lb} = 0.1$.

cedure [63, 64] could bring second order improvement of the normal calculations on regular grid. From the point of view of the numerical efficiency and adaptation to parallel calculations, the method is not essentially different from the ILB methods. In so far, locality of its main operations and linear increase of the computational efforts with space refining are advantageous for realistic calculations. Since no complicated discretization/advection/solution procedure is needed, the method can be easily implemented by the LB users and novices. First-order Chapman-Enskog expansion of the populations, which contains in itself all components of the strain tensor, allows local and simple incorporation of viscoelastic effects into the model. In particular, we combine the LB filling algorithm with the regularized Bingham model [1]. First results [23] are found in good agreement with the theoretical and the numerical predictions.

Besides other straightforward extensions of the method, for instance to other LB velocity models or to two (or more) fluids, several problems remain. The first one is related to intrinsic compressibility of the method. Robust applications of the method in complex geometries require to develop adaptive strategy for dynamic change of the LB parameters and introduce variable space resolution into the model. The second difficulty is observed in filling simulations at very small Reynolds numbers, e.g processing of metal alloys. We conjecture that the reason lies in inaccuracy of first order Chapman-Enskog approximation and/or boundary conditions in the limit of high LB viscosities ($\tau > 1$). Although the problem can be avoided by restriction of the LB viscosities to their reliable interval, the corresponding reduction in LB velocities slows the method. Finally, effective and accurate design of LB upwind schemes needs further investigation. Despite these difficulties, the method seems very promising for real-life simulations in injected molding provided that the conditions on its accuracy are met by a proper choice of the numerical parameters.

APPENDIX: GENERALIZED LATTICE BOLTZMANN EQUATION

In the first two sections, we present basis vectors and eigenvalues for $D2Q9$ and $D3Q15$ models. This is followed by common remarks and particular solutions for free eigenvalues in Section A.3. Details to implementation of collision step are discussed in Section A.4. First order term $\epsilon N_i^{(1)}$ is obtained in Section A.5 using notations of current paper.

A.1. MODEL $D2Q9$

Let nine velocities of the $D2Q9$ model be ordered as following: $(0,0)$, $(1,0)$, $(0,1)$, $(-1,0)$, $(0,-1)$, $(1,1)$, $(-1,1)$, $(-1,-1)$, $(1,-1)$. Orthonormal basis vectors

for $D2Q9$ can be chosen in the form (cf. rel.(12))

$$\mathbf{e}_1 = \frac{1}{3}\{C_i^0\}\ , \quad \mathbf{e}_2 = \frac{1}{\sqrt{6}}\{C_{ix}\}\ , \quad \mathbf{e}_3 = \frac{1}{\sqrt{6}}\{C_{iy}\}\ ,$$
$$\mathbf{e}_4 = 6\{t_p^\star C_{ix}C_{iy}\}\ , \quad \mathbf{e}_5 = 3\{t_p^\star(C_{ix}^2 - \frac{1}{2}c_i^2)\}\ ,$$
$$\mathbf{e}_6 = \sqrt{3}\{t_p^\star(C_{ix}^3 - 3C_{ix}C_{iy}^2)\}\ , \quad \mathbf{e}_7 = \sqrt{3}\{t_p^\star(C_{iy}^3 - 3C_{iy}C_{ix}^2)\}\ , \tag{A.1}$$
$$\mathbf{e}_8 = \frac{\mathbf{E^{im}}}{\parallel \mathbf{E^{im}} \parallel}\ , \ \mathbf{E^{im}} = \{t_p^\star \frac{c_i^2}{D} - r_p^\star\}\ , \ \parallel \mathbf{E^{im}} \parallel = \frac{1}{6}\sqrt{(41 - 138c_s^2 + 117c_s^4)}\ ,$$
$$\mathbf{e}_9 = \frac{\mathbf{T}_\mathrm{p}}{\parallel \mathbf{T}_\mathrm{p} \parallel}\ , \ T_0 = 4(1 - 3c_s^2)\ , \ T_1 = 13 - 21c_s^2\ , \ T_2 = 24c_s^2 - 14\ ,$$
$$\parallel \mathbf{T}_\mathrm{p} \parallel = 6\sqrt{(41 - 138c_s^2 + 117c_s^4)}\ . \tag{A.2}$$

where vector $\mathbf{T}_\mathrm{p}$ has constant value T_p for each p-class. Basis vectors (A.2) are similar to those in [24, 25, 38, 51], except the two last vectors. Let us refer here to two alternative, c_s^2-independent, basis vectors as $\mathbf{E}$ and $\mathbf{H}$:

$$E_i = \{3C_i^2 - 4\}\ , \ H_i = \{9C_{ix}^2C_{iy}^2 - 6C_i^2 + 4\}\ ,$$
$$E_i = -\frac{2}{\parallel \mathbf{E^{im}} \parallel}(-2 + 3c_s^2)\mathbf{e}_8 + \frac{36}{\parallel \mathbf{T}_\mathrm{p} \parallel}(-5 + 9c_s^2)\mathbf{e}_9\ ,$$
$$H_i = \frac{1}{\parallel \mathbf{E^{im}} \parallel}(-5 + 9c_s^2)\mathbf{e}_8 + \frac{72}{\parallel \mathbf{T}_\mathrm{p} \parallel}(-2 + 3c_s^2)\mathbf{e}_9\ . \tag{A.3}$$

The eigenvalues associated with basis vectors (A.2) are

$$\{0, 0, 0, \lambda_\psi^{\alpha\beta}, \lambda_\psi^{\alpha\alpha}, \lambda_2, \lambda_2, \lambda_e, \lambda_l\}\ . \tag{A.4}$$

When $\lambda_e = \lambda_l$, the system of basis vectors (A.2) is equivalent to those which use the vectors (A.2) with the corresponding equal eigenvalues. When $\lambda_\psi^{\alpha\beta} = \lambda_\psi^{\alpha\alpha}$, the projection of first order population expansion (10), (12) in standard coordinate system on the basis (A.2) yields the coefficients of the decomposition as (see first

terms for $(N_i^{\mathrm{eq}\cdot}, \mathbf{e}_k)$ an last term for $(N_i^{(1)}, \mathbf{e}_k)$, respectively):

$$
\begin{aligned}
&(\mathbf{N},\mathbf{e}_1) = \frac{1}{3}\rho\,, \quad (\mathbf{N},\mathbf{e}_2) = \frac{J_x}{\sqrt{6}}\,, \quad (\mathbf{N},\mathbf{e}_3) = \frac{J_y}{\sqrt{6}}\,,\\
&(\mathbf{N},\mathbf{e}_4) = \frac{j_x j_y}{2\rho} + \frac{1}{6}\frac{1}{\lambda_\psi}(\frac{\partial j_x}{\partial y} + \frac{\partial j_y}{\partial x})\,,\\
&(\mathbf{N},\mathbf{e}_5) = \frac{1}{2\rho}(j_x^2 - j_y^2) + \frac{1}{3\lambda_\psi}(\frac{\partial j_x}{\partial x} - \frac{\partial j_y}{\partial y})\,,\\
&(\mathbf{N},\mathbf{e}_6) = \frac{\sqrt{3}J_x}{6}\,, \quad (\mathbf{N},\mathbf{e}_7) = \frac{\sqrt{3}J_y}{6}\,, \qquad\qquad (A.5)\\
&(\mathbf{N},\mathbf{e}_8) = \alpha_8\rho + \beta_8\frac{(j_x^2+j_y^2)}{\rho} + \frac{1}{\parallel \mathbf{E^{im}} \parallel}\frac{1}{\lambda_e}(\frac{\partial j_x}{\partial x} + \frac{\partial j_y}{\partial y})\,,\\
&\qquad \alpha_8 = -\frac{1}{12\parallel \mathbf{E^{im}} \parallel}(39c_s^4 - 43c_s^2 + 12)\,,\ \beta_8 = -\frac{1}{12\parallel \mathbf{E^{im}} \parallel}(15c_s^2 - 9)\,,\\
&(\mathbf{N},\mathbf{e}_9) = \alpha_9\rho + \beta_9\frac{(j_x^2+j_y^2)}{\rho}\,,\\
&\qquad \alpha_9 = \frac{1}{\parallel \mathbf{T}_{\mathrm{p}} \parallel}(4 - 6c_s^2)\,,\ \beta_9 = \frac{3}{\parallel \mathbf{T}_{\mathrm{p}} \parallel}(3c_s^2 - 1)\,. \qquad\qquad (A.6)
\end{aligned}
$$

When $c_s^2 = \frac{1}{3}$, the data is: $\parallel \mathbf{E^{im}} \parallel = \frac{\sqrt{2}}{3}$, $\parallel \mathbf{T}_{\mathrm{p}} \parallel = 12\sqrt{2}$, $E_i = 3\sqrt{2}(\mathbf{e}_8 - \mathbf{e}_9)$, $H_i = -3\sqrt{2}(\mathbf{e}_8 + \mathbf{e}_9)$, $\alpha_8 = -\frac{\sqrt{2}}{4}$, $\beta_8 = \frac{\sqrt{2}}{2}$, $\alpha_9 = \frac{\sqrt{2}}{12}$, $\beta_9 = 0$.

A.2. *D3Q15* MODEL.

Let 15 velocities of the $D3Q15$ model be ordered as following: $(0,0,0)$, $(1,0,0)$, $(0,1,0)$, $(-1,0,0)$, $(0,-1,0)$, $(0,0,1)$, $(0,0,-1)$, $(1,1,1)$, $(-1,1,1)$, $(-1,-1,1)$, $(1,-1,1)$, $(1,1,-1)$, $(-1,1,-1)$, $(-1,-1,-1)$, $(1,-1,-1)$. Orthonormal vectors are chosen in the form (cf. rel.(12)), written in standard coordinate system

$$
\begin{aligned}
&\mathbf{e}_1 = \frac{1}{\sqrt{15}}\{C_i^0\}\,, \quad \mathbf{e}_2 = \frac{1}{\sqrt{10}}\{C_{ix}\}\,, \quad \mathbf{e}_3 = \frac{1}{\sqrt{10}}\{C_{iy}\}\,, \quad \mathbf{e}_4 = \frac{1}{\sqrt{10}}\{C_{iz}\}\,,\\
&\mathbf{e}_5 = 6\sqrt{2}\{t_p^\star C_{ix}C_{iy}\}\,, \quad \mathbf{e}_6 = 6\sqrt{2}\{t_p^\star C_{iy}C_{iz}\}\,, \quad \mathbf{e}_7 = 6\sqrt{2}\{t_p^\star C_{ix}C_{iz}\}\,,\\
&\mathbf{e}_8 = \frac{9}{2\sqrt{3}}\{t_p^\star(C_{ix}^2 - \frac{1}{D}c_i^2)\}\,, \quad \mathbf{e}_9 = \frac{3}{2}\{t_p^\star(C_{iy}^2 - C_{iz}^2)\}\,,\\
&\mathbf{e}_{10} = \frac{1}{\sqrt{8}}\{t_p^\star C_{ix}C_{iy}C_{iz}\}\,, \quad \mathbf{e}_{11} = \frac{3}{\sqrt{10}}\{t_p^\star(2C_{ix}^3 - 3C_{ix}(C_{iy}^2 + C_{iz}^2))\}\,,\\
&\mathbf{e}_{12} = \frac{3}{\sqrt{10}}\{t_p^\star(2C_{iy}^3 - 3C_{iy}(C_{ix}^2 + C_{iz}^2))\}\,, \qquad\qquad (A.7)\\
&\mathbf{e}_{13} = \frac{3}{\sqrt{10}}\{t_p^\star(2C_{iz}^3 - 3C_{iz}(C_{ix}^2 + C_{iy}^2))\}\,,\\
&\mathbf{e}_{14} = \frac{\mathbf{E^{im}}}{\parallel \mathbf{E^{im}} \parallel}\,,\ \mathbf{E^{im}} = \{t_p^\star\frac{c_i^2}{D} - r_p^\star\}\,,\ \parallel \mathbf{E^{im}} \parallel = \frac{1}{36}\sqrt{(1410 - 6660c_s^2 + 7938c_s^4)}\,,\\
&\mathbf{e}_{15} = \frac{\mathbf{T}_{\mathrm{p}}}{\parallel \mathbf{T}_{\mathrm{p}} \parallel}\,,\ T_0 = 2(5 - 21c_s^2)\,,\ T_1 = 25 - 57c_s^2\,,\ T_2 = -20 + 48c_s^2\,,\\
&\qquad \parallel \mathbf{T}_{\mathrm{p}} \parallel = \sqrt{30(235 - 1110c_s^2 + 1323c_s^4)}\,. \qquad\qquad (A.8)
\end{aligned}
$$

Here again, the constant multiple before the lattice vector corresponds to inverse of the norm of this vector. Basis vectors (A.6) are similar to those in [41], except the two last vectors. Let us refer here to two alternative, c_s^2-independent, basis vectors as $\mathbf{E}$ and $\mathbf{H}$:

$$
\begin{aligned}
&E_i = \{C_i^2 - 2\}\ ,\ H_i = \frac{1}{2}\{15C_i^4 - 55C_i^2 + 32\}\ ,\\
&E_i = \frac{1}{3\| \mathbf{E^{im}} \|}(-5 + 9c_s^2)\mathbf{e}_{14} - \frac{30}{\| \mathbf{T}_{\rm p} \|}(-11 + 27c_s^2)\mathbf{e}_{15}\ ,\\
&H_i = \frac{5}{3\| \mathbf{E^{im}} \|}(-11 + 27c_s^2)\mathbf{e}_{14} + \frac{120}{\| \mathbf{T}_{\rm p} \|}(-5 + 9c_s^2)\mathbf{e}_{15}\ .
\end{aligned}
\tag{A.9}
$$

Basis vectors (A.6) are associated with the following eigenvalues

$$
\{0, 0, 0, 0, \lambda_\psi^{\alpha\beta}, \lambda_\psi^{\alpha\beta}, \lambda_\psi^{\alpha\beta}, \lambda_\psi^{\alpha\alpha}, \lambda_\psi^{\alpha\alpha}, \lambda_{xyz}, \lambda_2, \lambda_2, \lambda_2, \lambda_e, \lambda_l\}\ . \tag{A.10}
$$

Same remarks as for (A.2) are valid here. In case $\lambda_\psi^{\alpha\beta} = \lambda_\psi^{\alpha\alpha}$, the coefficients of the decomposition on the basis (A.6) are related with the macroscopic quantities as

$$
\begin{aligned}
&(\mathbf{N}, \mathbf{e}_1) = \frac{\rho}{3\sqrt{5}}\ ,\quad (\mathbf{N}, \mathbf{e}_2) = \frac{J_x}{\sqrt{10}}\ ,\quad (\mathbf{N}, \mathbf{e}_3) = \frac{J_y}{\sqrt{10}}\ ,\quad (\mathbf{N}, \mathbf{e}_4) = \frac{J_z}{\sqrt{10}}\ ,\\
&(\mathbf{N}, \mathbf{e}_5) = \frac{j_x j_y}{2\sqrt{2}\rho} + \frac{1}{6\sqrt{2}}\frac{1}{\lambda_\psi}(\frac{\partial j_x}{\partial y} + \frac{\partial j_y}{\partial x})\ ,\\
&(\mathbf{N}, \mathbf{e}_6) = \frac{j_y j_z}{2\sqrt{2}\rho} + \frac{1}{6\sqrt{2}}\frac{1}{\lambda_\psi}(\frac{\partial j_y}{\partial z} + \frac{\partial j_z}{\partial y})\ ,\\
&(\mathbf{N}, \mathbf{e}_7) = \frac{j_x j_z}{2\sqrt{2}\rho} + \frac{1}{6\sqrt{2}}\frac{1}{\lambda_\psi}(\frac{\partial j_x}{\partial z} + \frac{\partial j_z}{\partial x})\ ,\\
&(\mathbf{N}, \mathbf{e}_8) = \frac{(2j_x^2 - (j_y^2 + j_z^2)}{2\sqrt{3}\rho} + \frac{\sqrt{3}}{9\lambda_\psi}(2\frac{\partial j_x}{\partial x} - (\frac{\partial j_y}{\partial y} + \frac{\partial j_z}{\partial z}))\ ,\\
&(\mathbf{N}, \mathbf{e}_9) = \frac{(j_y^2 - j_z^2)}{2\rho} + \frac{1}{3}\frac{1}{\lambda_\psi}(\frac{\partial j_y}{\partial y} - \frac{\partial j_z}{\partial z})\ ,\\
&(\mathbf{N}, \mathbf{e}_{10}) = 0\ ,\quad (\mathbf{N}, \mathbf{e}_{11}) = \frac{7J_x}{6\sqrt{10}}\ ,\quad (\mathbf{N}, \mathbf{e}_{12}) = \frac{7J_y}{6\sqrt{10}}\ ,\quad (\mathbf{N}, \mathbf{e}_{13}) = \frac{7J_z}{6\sqrt{10}}\ ,\\
&(\mathbf{N}, \mathbf{e}_{14}) = \alpha_{14}\rho + \beta_{14}\frac{(j_x^2 + j_y^2 + j_z^2)}{\rho} + \frac{1}{\| \mathbf{E^{im}} \|}\frac{1}{\lambda_e}(\frac{\partial j_x}{\partial x} + \frac{\partial j_y}{\partial y} + \frac{\partial j_z}{\partial z})\ ,\\
&\qquad \alpha_{14} = -\frac{1}{72\| \mathbf{E^{im}} \|}(441c_s^4 + 72 - 353c_s^2)\ ,\ \beta_{14} = -\frac{1}{72\| \mathbf{E^{im}} \|}(57c_s^2 - 25)\ ,\\
&(\mathbf{N}, \mathbf{e}_{15}) = \alpha_{15}\rho + \beta_{15}\frac{(j_x^2 + j_y^2 + j_z^2)}{\rho}\ ,\\
&\qquad \alpha_{15} = \frac{2}{\| \mathbf{T}_{\rm p} \|}(5 - 11c_s^2)\ ,\ \beta_{15} = \frac{10}{\| \mathbf{T}_{\rm p} \|}(3c_s^2 - 1)\ .
\end{aligned}
\tag{A.11, A.12}
$$

Similar as above, vector $\mathbf{N} - \mathbf{N}^{\rm eq.}$ has no projection on first four vectors, corresponding to mass and momentum and the corresponding terms can be omitted in summation in Eq.(5). When $c_s^2 = \frac{1}{3}$, the data is $\| \mathbf{E^{im}} \| = \frac{\sqrt{2}}{6}$, $\| \mathbf{T}_{\rm p} \| = 6\sqrt{10}$, $E_i = -2\sqrt{2}\mathbf{e}_{14} + \sqrt{10}\mathbf{e}_{15}$, $H_i = -10\sqrt{2}\mathbf{e}_{14} - 4\sqrt{10}\mathbf{e}_{15}$, $\alpha_{14} = -\frac{5\sqrt{2}}{36}$, $\beta_{14} = \frac{\sqrt{2}}{4}$, $\alpha_{15} = \frac{2\sqrt{10}}{45}$, $\beta_{15} = 0$.

A.3. REMARKS ON CHOICE OF THE FREE EIGENVALUES

The basis vectors above are mainly chosen among the polynomial vectors coming into Chapman-Enskog expansion. In case of more general model considered in [24, 25, 38], the eigenvalues $\lambda_\psi^{\alpha\beta}$ and $\lambda_\psi^{\alpha\alpha}$ can differ under condition that the equilibrium function is modified in order to recover the correct stress-tensor term in the derived Navier-Stokes equations. Similar generalization [20] is done for $D3Q15$ Model. In this paper, we assume $\lambda_\psi^{\alpha\beta}$ and $\lambda_\psi^{\alpha\alpha}$ to be equal and denote them as λ_ψ. Eigenvalues λ_e and λ_ψ enter as the coefficients into first order expansion (cf. (12)) and therefore, determine the transport coefficients (15a) and (15b). Other eigenvalues are free.

"Magic solution" for free eigenvalues relates the eigenvalues associated with the odd order polynomial eigenvectors ($\lambda_\mathcal{O} = \{\lambda_2, \lambda_{xyz}\}$) to those associated with the even order polynomials ($\lambda_\mathcal{E} = \{\lambda_\psi, \lambda_e, \lambda_l\}$) through "magic" condition

$$\lambda_\mathcal{O}(\lambda_\mathcal{E}) = -8\frac{\lambda_\mathcal{E} + 2}{\lambda_\mathcal{E} + 8}\,. \tag{A.13}$$

Its properties are discussed in Section 4.1. When the non-linear term is present at equilibrium (10), the solution (A.13) is not more exact for Poiseuille flow until "free" projection $\alpha\mathbf{H}$ is introduced into the equilibrium function

$$\mathbf{N}^{\mathrm{eq}\cdot} \to \mathbf{N}^{\mathrm{eq}\cdot} + \alpha\mathbf{H}\,. \tag{A.14}$$

Here, α is some constant and $\mathbf{H}$ is given by relation (A.2) for the $D2Q9$ Model and by relation (A.8) for the $D3Q15$ Model. Important here that equilibrium projection on $\mathbf{H}$ does not influence the derived Navier-Stokes equations. The coefficient α can be used to annihilate the contribution of a non-linear term in $\epsilon N_i^{(1)}$. In particular, when

$$\alpha = \frac{1}{12}(j_x^2 + j_y^2)\,, \quad \text{for} \quad D2Q9\,, \tag{A.15a}$$

$$\alpha = -\frac{1}{24}(j_x^2 + j_y^2 + j_z^2)\,, \quad \text{for} \quad D3Q15\,, \tag{A.15b}$$

such a term vanishes when $\boldsymbol{j}$ has only one non-zero component, e.g. Poiseuille flow. In terms of equilibrium weights, solution (A.15a) means that the projection of equilibrium in a form (10) is doubled in 2D: $(\mathbf{N}^{\mathrm{eq}\cdot} + \alpha\mathbf{H}, \mathbf{H}) = 2(\mathbf{N}^{\mathrm{eq}\cdot}, \mathbf{H})$. This coincides with the solution obtained with another approach by D.d'Humières [40]. In 3D, we have $(\mathbf{N}^{\mathrm{eq}\cdot} + \alpha\mathbf{H}, \mathbf{H}) = 4(\mathbf{N}^{\mathrm{eq}\cdot}, \mathbf{H})$. Numerical computations confirm that when $\alpha\mathbf{H}$ is added to equilibrium, momentum definition (3b) is used, and magic solution (A.13) is employed for free eigenvalues, Poiseuille profile in a channel of given width is obtained exactly, likely as in case of linear equilibrium function.

"First order solution" for free eigenvalues puts all eigenvalues except λ_ψ equal to -1:

$$\lambda_2 = \lambda_e = \lambda_{xyz} = \lambda_l = -1\,. \tag{A.16}$$

In this case, only the projection on second order polynomial basis vectors associated with λ_ψ does not vanish after collision. This becomes especially transparent when

the collision is written in the equivalent form:

$$\tilde{N}_i(\boldsymbol{r},t) = N_i^{\mathrm{eq.}}(\boldsymbol{r},t) + \sum_{k=0}^{b_m}(1+\lambda_k)(\mathbf{N}-\mathbf{N}^{\mathrm{eq.}},\mathbf{e}_k)e_{ki}\ . \tag{A.17}$$

While using Chapman-Enskog expansion at reconstruction step, we neglect $O(\epsilon^2)$ and $O(\mathrm{M}^2)$ terms associated with the eigenvalues λ_e and free eigenvalues. Assuming that first order collision could dump the oscillations in these terms, we often use it for calculations in this paper.

A.4. IMPLEMENTATION OF COLLISION

Equation (5) is formulated in terms of the normalized basis vectors in order to simplify the notations. It is much more numerically efficient to represent basis vectors as the vectors with integer components, say $\mathbf{e}_k^{\mathrm{int}}$. This enables us to compute easily all equal linear combinations which come into projection and into the decomposition: $\phi_k = 1/\| \mathbf{e}_k^{\mathrm{int}} \|^2 \times (\mathbf{N},\mathbf{e}_k^{\mathrm{int}})$ and $\sum_k \phi_k \mathbf{e}_k^{\mathrm{int}}$, accordingly. Moreover, computing the generalized collision (5) does not require the evaluation of equilibrium function in a form (10). Following idea [40], one can represent it in a form of equilibrium projection. The collision reads then

$$\tilde{\mathbf{N}}(\boldsymbol{r},t) = \mathbf{N}(\boldsymbol{r},t) + \sum_{k=0}^{b_m}\lambda_k\{\phi_k - \phi_k^{\mathrm{eq.}}\}\mathbf{e}_k^{\mathrm{int}}\ ,\ \phi_k^{\mathrm{eq.}} = (\mathbf{N}^{\mathrm{eq.}},\mathbf{e}_k^{\mathrm{int}})\ . \tag{A.18}$$

Since $\phi_k^{\mathrm{eq.}}$ can be computed analytically (see (A.4) and (A.10)), the computational efforts reduce drastically (at least at factor two) and become quite comparable with the BGK collision where the equilibrium (10) should be computed. Nevertheless, when the equilibrium is computed for some other purpose as well, first order collision is relatively fast. A particular fastest choice $\lambda_k \equiv -1$ is employed in [82]. In case of convergence to stationary state, however, a proper choice of the eigenvalues reduces drastically the number of time steps without loss of the accuracy.

A.5. FIRST ORDER EXPANSION

We precise here how we obtain first order correction to equilibrium $\epsilon N_i^{(1)}$ in the form (12) in the standard coordinate system. Following [13], Chapman-Enskog expansion (9) $\partial_t = \epsilon\partial_{t_1} + \epsilon^2\partial_{t_2}$, $\partial_x = \epsilon\partial_{\bar{x}}$ leads to ϵ^1-accurate macroscopic relations:

$$\partial_{t_1}\rho + \nabla'\cdot j_\alpha = 0\ , \tag{A.19a}$$

$$\partial_{t_1} j_\alpha + \partial_{\bar{\beta}} P_{\alpha\beta} = 0\ ,\ P_{\alpha\beta} = c_s^2\rho\delta_{\alpha\beta} + \rho u_\alpha u_\beta\ . \tag{A.19b}$$

Correction $N_i^{(1)}$ satisfies first order Taylor development of the Eq. (5):

$$\partial_{t_1} N_i^{\mathrm{eq.}} + C_{i\alpha}\partial_{\bar{\alpha}} N_i^{\mathrm{eq.}} = \sum_{j=0}^{b_m}\mathsf{A}_{ij}N_j^{(1)}\ ,\qquad i\in\{0,\dots,b_m\}\ . \tag{A.20}$$

Substitution of the relation (10) into (A.20) yields with help of the relations (A.19a),(A.19b) and when $O(u^2)$ and $O(\epsilon^2)$ terms are neglected:

$$\begin{aligned}\partial_{t_1} N_i^{\mathrm{eq.}} + C_{i\alpha}\partial_{\bar{\alpha}} N_i^{\mathrm{eq.}} &= C_{i\alpha} t_p^\star [\overbrace{\partial_{t_1} j_\alpha + c_s^2 \partial_{\bar{\alpha}} \rho}^{=0}] + r_p^\star \partial_{t_1}\rho + \frac{\partial j_\alpha}{\partial \beta'} t_p^\star C_{i\alpha} C_{i\beta} \\ &= \nabla' \cdot \boldsymbol{j}(t_p^\star \frac{c_i^2}{D} - r_p^\star) + \frac{\partial j_\alpha}{\partial \beta'} t_p^\star (C_{i\alpha}C_{i\beta} - \frac{c_i^2}{D}\delta_{\alpha\beta}) \quad (A.21)\end{aligned}$$

By using the definitions in (12), relation (A.20) becomes

$$\epsilon \sum_{j=0}^{b_m} \mathsf{A}_{ij} N_j^{(1)} = \frac{\partial j_\alpha}{\partial \beta} Q_{i\alpha\beta} + \nabla \cdot \boldsymbol{j} E_i^{\mathrm{im}} \; . \qquad (A.22)$$

Replacing $\{\alpha, \beta\}$ by $\{\alpha', \beta'\}$, the derivation in any other coordinate system follows exactly the same lines. Relation (A.22) takes then more general form

$$\epsilon \sum_{j=0}^{b_m} \mathsf{A}_{ij} N_j^{(1)} = \frac{\partial j_\alpha}{\partial \beta'} Q_{i\alpha'\beta'} + \nabla \cdot \boldsymbol{j} E_i^{\mathrm{im}} \; . \qquad (A.23)$$

Since the vectors $\{Q_{i\alpha'\beta'}\}$ are fully decomposed on the second order polynomial basis vectors associated with the eigenvalue λ_ψ and vector $\mathbf{E}^{\mathrm{im}}$ is chosen to be a basis vector associated with the eigenvalue λ_e, relation (A.23) takes a form (12).

ACKNOWLEDGMENTS

The main part of this work has been founded by the join project "Parallele Partikelcodes für industrielle Anwendungen" between the BMBF and the companies MAGMA Giessereitechnologie GmbH, Aachen, NEUMAG-Neumünstersche Maschinen- und Anlagenbau GmbH, Neumünster und FILTERWERK MANN+HUMMEL GmbH, Speyer. We acknowledge MAGMA GmbH for very helpful conceptual and practical input as well as their technical support for using MAGMASOFT parameter data base, pre- and post- processing tools. A final part of this work was supported by DFG Project "Die verallgemeinerte Lattice Boltzmann Methode fr freie Randwertprobleme und Mehrphasenstrmungen". A special thank is given to P. Klein for parallelization of the code. The authors are grateful to M. Beck, R. Haag, D. d'Humières, J. Linn, M. D. Lipinski, J. Kuhnert, C. Lojewski, F. J. Pfreundt, D. Reinel-Bitzer, W. Schäffer and S. Tiwari for useful discussions and aid.

REFERENCES

1. A. N. Alexandrou, E. Duc, and V. Entov, Inertial, viscous and yield stress effects in Bingham fluid filling of a 2-D cavity, *Journal of Non-Newtonian Fluid Mechanics* **96 (3)**, 383 (2001).
2. M. Bakhudarov, H. You, J. Ortega, J. Beech, S. B. Chin, and D. H. Kirkwood, Experimental Validation and Development of FLOW-3D for Casting Problems, In: *Modeling of Casting Welding and Advanced Solidification Processes- VI, Proc. VI th. Int. Conf.* 1993, Palm Beach, FL, TMS, AIME, 441 (1993).
3. A. N. Brooks and T. J. R. Hughes, Streamline upwind/Petrov-Galerkin formulations for convection dominated flows with particular emphasis on the incompressible Navier-Stokes equations, *Computer Methods in Applied Mechanics and Engineering* **32**, 199 (1982).
4. J. M. Buick and C. A. Greated, Gravity in a lattice Boltzmann model, *Physical Review E* **61**, 5307 (2000).
5. C. Cercignani, *Mathematical Methods in Kinetic Theory* (Macmillan, 1969).
6. H. Chen, C. Teixeira, and K. Molvig, Realization of Fluid Boundary Conditions via Discrete Boltzmann Dynamics, *Int. J. of Mod. Phys.* **9**, 1281 (1998).

7. S. Chen, Z. Wang, X. Shan, and Gary D. Doolen, Lattice Boltzmann computational fluid dynamics in three dimensions, *J. Stat. Phys.* **68**, 378 (1992).

8. S. Chen and G. D. Doolen, Lattice Boltzmann method for fluid flows, *J. Fluid Mech.* **30**, 329 (1998).

9. I. Christie, D. F. Griffiths, A. R. Mitchell, and O. C. Zienkiewicz, Finite element methods for second order differential equations with significant first derivatives, *International Journal for Numerical Methods in Engineering* **10**, 1389 (1976).

10. High pressure die casting simulation using Smoothed Particle Hydrodynamics, *J. Cast Metals Res.* **12**, 335 (2000).

11. R. Cornubert, D. d'Humières, and D. Levermore, A Knudsen layer theory, *Physica D* **47**, 241 (1991).

12. O. Filippova and D. Hänel, Boundary-fitting and local grid refinement for Lattice-BGK models, *Int. J. Mod. Phys.* **9**, 1271 (1998).

13. U. Frisch, D. d'Humiéres, B. Hasslacher, P. Lallemand, Y. Pomeau, and J. -P. Rivet, Lattice gas hydrodynamics in two and three dimensions, *Complex Systems* **1**, 649 (1987).

14. D. E. Fyfe, E.S. Oran, and M. J. Fritts, Surface tension and viscosity with Lagrangian hydrodynamics on a triangular mesh, *J. Comput. Phys.* **76**, 394 (1988).

15. O. S. Galaktionov, P. D. Anderson, G. W. M. Peters, and F. N. Van de Vosse, An adaptive front tracking technique for three-dimensional transient flows, *Int. J. Numer. Methods Fluids* **32**, 201 (2000).

16. D. M. Gao, A three-dimensional hybrid finite element-volume tracking model for mold filling in casting processes, *Int. J. Numer. Methods Fluids* **29**, 877 (1999).

17. I. Ginzbourg and P. M. Adler, Boundary flow condition analysis for three-dimensional lattice Boltzmann model, *J. Phys. II France* **4**, 191 (1994).

18. I. Ginzbourg and P. M. Adler, Boundary conditions at a plane liquid-liquid interface in FCHC lattice Boltzmann model, (unpublished, 1994). I. Ginzbourg and P. M. Adler, Surface tension models with different viscosities, *Transport in Porous Media* **20**, 37 (1995).

19. I. Ginzbourg and D. d'Humières, Local second-order boundary method for Lattice Boltzmann models, *J. Stat. Phys.* **84**, (5/6), 927 (1996). I. Ginzbourg and D. d'Humières, Local second-order boundary method for Lattice Boltzmann models. Part II. Application to complex geometries, (unpublished, 1996).

20. I. Ginzburg, General second order Chapman-Enskog expansion for Lattice Boltzmann models, (unpublished, 1999).

21. I. Ginzburg and G. Wittum, Two-Phase flows on interface refined grids modeled with VOF, staggered finite volumes, and spline interpolants, *J. Comput. Phys.* **166**, 302 (2001).

22. I. Ginzburg, "Introduction of upwind and free boundary into lattice Boltzmann method", in *Discrete Modelling and Discrete Algorithms in Continuum Mechanics* (eds. T. Sonar & I. Thomas), pp. 97–109 (Logos-Verlag, Berlin, 2001).

23. I. Ginzburg et K. Steiner, A free surface lattice-Boltzmann method for modelling the filling of expanding cavities by Bingham Fluids, to appear in *Phil. Trans. R. Soc. Lond. A*, (2002).

24. L. Giraud, D. d'Humières, and P. Lallemand, A lattice Boltzmann model for Jeffreys viscoelastic fluid, *Europhys. Lett.* **42**, 625 (1998).

25. L.Giraud, Fluides visco-élastiques par la méthode de Boltzmann sur réseau, *PhD, Université Paris VI*, 1997.

26. D. Wolf-Gladrow, Lattice gas cellular automata and lattice Boltzmann models: an introduction (Springer, 2000, Lecture notes in mathematics, 1725, ISBN 3-540-66973-6).

27. A. K. Gunstensen, D. H. Rothmann, S. Zaleski, and G. Zanetti, Lattice Boltzmann model of immiscible fluids , *Phys. Rev. A* **43**, No 8, 4320 (1991).

    A. K. Gunstensen and D. H. Rothmann, *Europhys. Lett.* **18**, 157 (1992); *J. Geophys. Res.* **98**, 6431(1993).

28. *Injection Molding Handbook : The Complete Molding Operation: Technology, Performance, Economics*, (Van Nostrand Reinhold, NewYork, 1986).

29. Xiaoyi He, Yisu Zou, Li-Shi Luo, and Micah Dembo, Analytic solutions of simple flows and analysis of nonslip boundary conditions for the Lattice Boltzmann BGK model, *J. Stat. Phys.* **87**, 913 (1997).

30. X. He and Li-Shi Luo, A priori derivation of the Lattice Boltzmann equation, *Phys. Rev. E* **55**, R6333 (1997).

31. X. He, S. Chen, and Raoyang Zhang, A Lattice Boltzmann scheme for incompressible multiphase flow and its application in simulation of Rayleigh-Taylor instability, *J. Comput. Phys.* **152**, 642 (1999).

32. F. J. Higuera and J. Jimenez, Boltzmann approach to lattice gas simulations, *Europhys. Lett.* **9**, 663 (1989).

33. F. Higuera, S. Succi, and R. Benzi, Lattice gas dynamics with enhanced collisions, *Europhys. Lett.* **9**, 345 (1989).

34. C. W. Hirt and B. D. Nicholls, Volume of fluid (VOF) method for the dynamics of free boundaries, *J. Comput. Phys.* **39**, 201 (1981).

35. C. W. Hirt, A Flow-3D study of the importance of fluid momentum in mold filling, *Num. Sim. of Casting Solidification in Automotive Applications. The Minerals, Metals and Material Society* (1991).

36. C. W. Hirt and R. P. Harper, Flow modeling for casting analysis, Technical Note FSI-88-TN7, Flow Science Int., Los Alamos, NM, 1988.

37. S. Hou, J. Sterling, S. Chen, and G. D. Doolen, A Lattice Boltzmann subgrid model for high Reynolds number flows, *Fields Institute Communications* **6**, 151 (1996).

38. D. d'Humières, Generalized Lattice-Boltzmann equations, AIAA Rarefied Gas Dynamics: Theory and Simulations, *Progress in Austronautics and Aeronautics* **59**, 450 (1992).

39. D. d'Humières, I. Ginzburg, and L. Giraud, Effective Lattice Boltzmann models for porous media, in preparation (2001).

40. D.d'Humières, private communications.

41. D. d'Humières, I. Ginzburg, M. Krafczyk, P. Lallemand et L.-S. Luo, Multiple-relaxation-time lattice Boltzmann models in three dimensions, to appear in *Phil. Trans. R. Soc. Lond. A* (2002).

42. J. H. Jeong and D. Y. Yang, Finite element analysis of transient fluid flow with free surface using VOF (VOLUME-OF-FLUID) method and adaptive grid, *Int. J. Numer. Methods Fluids* **26**, 1127 (1998).

43. I. V. Karlin, A. Ferrante, and H. C. Öttinger, Perfect entropy functions of the Lattice Boltzmann method, *Europhys. Lett.* **47(2)**, 182 (1999).

44. J. Kuhnert and S. Tiwari, private communications.

45. P. Klein, Scalable parallel software by chromatic ordered communications patterns, *Institut für Techno- und Wirtschaftsmathematik*, Annual Report, Kaiserslautern, (1999).

46. D. Kehrwald, Numerical Analysis of Immiscible Lattice BGK, PhD thesis, Kaiserslautern, 2002.

47. D. B. Kothe, Perspective on Eulerian finite volume methods for incompressible interfacial flows. *available at http://lune.mst.lanl.gov/Telluride/Text/publications.html.*

48. D. Kothe, D. Juric, K. Lam, and B. Lally, *Numerical receipes for mold filling simulation,* The Minerals, Metals and Materials Society, 17 (1998). [In: *Modeling of Casting Welding and Advanced Solidification Processes-VIII,* edited by B.G.Thomas and C.Beckermann].

49. A. J. C. Ladd, Numerical simulations of particulate suspensions via a discretized Boltzmann equation. Part 2. Numerical results, *J.Fluid Mech.* **271**, 311 (1994).

50. B. Lafaurie, C. Nardone, R. Scardovelli and S. Zaleski, Modeling Merging and Fragmentation in Multiphase Flows with SURFER, *J. Comput. Phys.* **113**, 134 (1994).

51. P. Lallemand and Li-Shi Luo, Theory of the Lattice Boltzmann method: dispersion, dissipation, isotropy, Galilean invariance, and stability, *Phys.Rev.E* **61**, 6546 (2000).

52. J. Li, Calcul d'Interface Affine par Morceaux, *C. R. Acad. Sci. Paris* **320**, série IIb, 391 (1995).

53. M. D. Lipinski, *Mold filling simulation for casting processes,* PhD, Aachen, 1996.

54. N. Lock, M. Jaeger, M. Medale, and R. Occelli, Local mesh adaptation technique for front tracking problems, *Int. J. Numer. Methods Fluids* **28**, 719 (1998).

55. Li-Shi Luo, Theory of the Lattice Boltzmann method: Lattice Boltzmann models for non-ideal gases, *Phys. Rev. E* **62**, 4982 (2000).

56. F. Mashayek and N. Ashgriz, A hybrid finite-element-volume-of-fluid method for simulating free surface flows and interfaces, *Int. J. Numer. Methods Fluids* **20**, 1363 (1995).

57. J. C. Maxwell, Phil. Trans. Royal Soc. I, Appendix(1879), in Scientific Papers of J. C. Maxwell, Dover Pub., 1965.

58. J. J. Monaghan, Simulating free surface flows with SPH, *J.Comput.Phys.* **110**, 399 (1994).

59. Renwei Mei, Li-Shi Luo, and Wei Shyy, An accurate curved boundary treatment in the Lattice Boltzmann method, *J. Comput. Phys.* **155**, 307 (1999).

60. S. J. Mosso, B. K. Swartz, D. B. Kothe, and S. P. Clancy, Recent enhancements of volume tracking algorithm for irregular grids, (Los Alamos National Laboratory, Los Alamos, NM, LA_UR_96_277, 1996), presented at the Parallel CFD Conference, Capri, Italy (March 20-23, 1996).

61. S. J. Mosso, B. K. Swartz, D. B. Kothe, and R. C. Ferrell, A parallel, volume-tracking algorithm for unstructured meshes, *Los Alamos National Laboratory, Los Alamos, NM, LA_UR_96_2420*, 1996.

62. X. Nie, Y.Qian, G.D. Doolen, and S. Chen, Lattice Boltzmann simulation of the two-dimensional Rayleigh-Taylor instability, *Phys. Rev. E* **58, 5**, 6861-6864(1998).

63. J.E. Jr. Pilliod and E. G. Puckett, Second order accurate volume-of-fluid algorithms for tracking material interfaces, *Technical report, Lawrence Berkeley National Laboratory, No.LBNL-40744*.

64. E. G. Puckett, A. S. Almgren, J. B. Bell, D. L. Marcus, and W. J. Rider, A high-order projection method for tracking fluid interfaces in variable density incompressible flows, *J. Comput. Phys.* **79**, 12 (1988).

65. G. R. Price, G. T. Reader, R. D. Rowe, and J. D. Bugg, *A Piecewise Parabolic Interface Calculations for volume Tracking,* Proceedings of the Sixth Annual Conference of the Computational Fluid/Dynamics Society of Canada, University of Victoria, Victoria, British/Columbia, (1998).

66. W. H. Press, S. A. Teukolsky, W. T. Wetterling, and B. P. Flannnery, Numerical Recipes in C. (Cambridge Univ. Press, Cambridge, UK, 1992).

67. Y. H. Qian, D. d'Humières, and P. Lallemand, Lattice BGK models for Navier-Stokes equation, *Europhys. Lett.* **17**, 479 (1992).

68. W. J. Rider and D. B. Kothe, Reconstructing volume tracking, *J. Comput. Phys.* **141**, 112 (1998).

69. M. Rudman, Volume tracking methods for interfacial flow calculations, *Int. J. Numer. Methods Fluids* **24**, 671 (1997).

70. M. Rudman, Volume tracking methods for incompressible multifluid flows with large density variations, *Int. J. Numer. Methods Fluids* **28**, 357 (1998).

71. D. H. Rothman and S. Zaleski, Lattice-gas models of phase separation: interfaces, phase transitions, *Rev. Mod. Phys.* **66**, 1417 (1994).

72. D. H. Rothmann and S. Zaleski, Lattice gas dynamics automata - simple model for complex hydrodynamics, Camb. Univ. Press, ISBN: 0-521-55201-X, (1997).

73. B. Sirrel, M. Holiday, and J. Campbell, *The Benchmark Test 1995,* In: Modeling of Casting Welding and Advanced Solidification Processes-VII, Proc.VII th. Int.Conf.,TMS,AIME, 915 (1995).

74. T. Sato and S. M. Richardson, Numerical simulation method for viscoelastic flow with free surfaces-fringe element generation method, *Int. J. Numer. Methods Fluids* **26**, 555 (1994).

75. R. Scardovelli and S. Zaleski, Direct numerical simulation of free-surface and interfacial flow, *Ann. Rev. Fluid Mech.* **31**, 567 (1999).

76. M. Schelkle, M. Rieber, and A. Frohn, Comparison of Lattice Boltzmann and Navier-Stokes simulations of three-dimensional free surface flows, *FED-VOL.236, Proceedings of the ASME*, Book No.H01072-1996.

77. J. D. Sterling and S. Chen, Stability analysis of Lattice Boltzmann methods, *J. Comput. Phys.* **123**, 196 (1996).

78. S. Succi, R. Benzi, F. Higuera, The lattice Boltzmann equation: a new tool for computational fluid dynamics, *Physica D.* **47**, 219 (1991).

79. M. Sussmann and P. Smereka, Axisymmetric free boundary problems, *J. Fluid Mech.* **341**, 269 (1997).

80. B. Swartz, The second order sharpening of blurred smooth borders, *Math. Comput.* **52**, 675 (1989).

81. S. H. Unverdi and G. Tryggvason, A front-tracking method for viscous, incompressible, multi-fluid flows, *J. Comput. Phys.* **100**, 25 (1992).

82. R. Verberg and A. J. C. Ladd, Simulation of low-Reynolds-number flow via a time-independent lattice-Boltzmann method, *Phys. Rev. E* **60**, 3366 (1999).

83. R. A. Worthing, J. Mozer, and G. Seeley, Stability of lattice Boltzmann methods in hydrodynamic regimes, *Phys. Rev. E* **56**, 2243 (1997).

84. D. L. Youngs, Time-dependent multi-material flow with large fluid distortion, In: *Numerical Methods for Fluid Dynamics*, edited by K. W. Morton and M. L. Norman, 1986.

Bisher erschienene Berichte des Fraunhofer ITWM

Die PDF-Files der folgenden Berichte finden Sie unter:
www.itwm.fhg.de/zentral/berichte.html

1. D. Hietel, K. Steiner, J. Struckmeier

A Finite - Volume Particle Method for Compressible Flows

We derive a new class of particle methods for conservation laws, which are based on numerical flux functions to model the interactions between moving particles. The derivation is similar to that of classical Finite-Volume methods; except that the fixed grid structure in the Finite-Volume method is substituted by so-called mass packets of particles. We give some numerical results on a shock wave solution for Burgers equation as well as the well-known one-dimensional shock tube problem.
(19 S., 1998)

2. M. Feldmann, S. Seibold

Damage Diagnosis of Rotors: Application of Hilbert Transform and Multi-Hypothesis Testing

In this paper, a combined approach to damage diagnosis of rotors is proposed. The intention is to employ signal-based as well as model-based procedures for an improved detection of size and location of the damage. In a first step, Hilbert transform signal processing techniques allow for a computation of the signal envelope and the instantaneous frequency, so that various types of non-linearities due to a damage may be identified and classified based on measured response data. In a second step, a multi-hypothesis bank of Kalman Filters is employed for the detection of the size and location of the damage based on the information of the type of damage provided by the results of the Hilbert transform.
Keywords:
Hilbert transform, damage diagnosis, Kalman filtering, non-linear dynamics
(23 S., 1998)

3. Y. Ben-Haim, S. Seibold

Robust Reliability of Diagnostic Multi-Hypothesis Algorithms: Application to Rotating Machinery

Damage diagnosis based on a bank of Kalman filters, each one conditioned on a specific hypothesized system condition, is a well recognized and powerful diagnostic tool. This multi-hypothesis approach can be applied to a wide range of damage conditions. In this paper, we will focus on the diagnosis of cracks in rotating machinery. The question we address is: how to optimize the multi-hypothesis algorithm with respect to the uncertainty of the spatial form and location of cracks and their resulting dynamic effects. First, we formulate a measure of the reliability of the diagnostic algorithm, and then we discuss modifications of the diagnostic algorithm for the maximization of the reliability. The reliability of a diagnostic algorithm is measured by the amount of uncertainty consistent with no-failure of the diagnosis. Uncertainty is quantitatively represented with convex models.
Keywords:
Robust reliability, convex models, Kalman filtering, multi-hypothesis diagnosis, rotating machinery, crack diagnosis
(24 S., 1998)

4. F.-Th. Lentes, N. Siedow

Three-dimensional Radiative Heat Transfer in Glass Cooling Processes

For the numerical simulation of 3D radiative heat transfer in glasses and glass melts, practically applicable mathematical methods are needed to handle such problems optimal using workstation class computers. Since the exact solution would require super-computer capabilities we concentrate on approximate solutions with a high degree of accuracy. The following approaches are studied: 3D diffusion approximations and 3D ray-tracing methods.
(23 S., 1998)

5. A. Klar, R. Wegener

A hierarchy of models for multilane vehicular traffic
Part I: Modeling

In the present paper multilane models for vehicular traffic are considered. A microscopic multilane model based on reaction thresholds is developed. Based on this model an Enskog like kinetic model is developed. In particular, care is taken to incorporate the correlations between the vehicles. From the kinetic model a fluid dynamic model is derived. The macroscopic coefficients are deduced from the underlying kinetic model. Numerical simulations are presented for all three levels of description in [10]. Moreover, a comparison of the results is given there.
(23 S., 1998)

Part II: Numerical and stochastic investigations

In this paper the work presented in [6] is continued. The present paper contains detailed numerical investigations of the models developed there. A numerical method to treat the kinetic equations obtained in [6] are presented and results of the simulations are shown. Moreover, the stochastic correlation model used in [6] is described and investigated in more detail.
(17 S., 1998)

6. A. Klar, N. Siedow

Boundary Layers and Domain Decomposition for Radiative Heat Transfer and Diffusion Equations: Applications to Glass Manufacturing Processes

In this paper domain decomposition methods for radiative transfer problems including conductive heat transfer are treated. The paper focuses on semi-transparent materials, like glass, and the associated conditions at the interface between the materials. Using asymptotic analysis we derive conditions for the coupling of the radiative transfer equations and a diffusion approximation. Several test cases are treated and a problem appearing in glass manufacturing processes is computed. The results clearly show the advantages of a domain decomposition approach. Accuracy equivalent to the solution of the global radiative transfer solution is achieved, whereas computation time is strongly reduced.
(24 S., 1998)

7. I. Choquet

Heterogeneous catalysis modelling and numerical simulation in rarified gas flows Part I: Coverage locally at equilibrium

A new approach is proposed to model and simulate numerically heterogeneous catalysis in rarefied gas flows. It is developed to satisfy all together the following points:
1) describe the gas phase at the microscopic scale, as required in rarefied flows,
2) describe the wall at the macroscopic scale, to avoid prohibitive computational costs and consider not only crystalline but also amorphous surfaces,
3) reproduce on average macroscopic laws correlated with experimental results and
4) derive analytic models in a systematic and exact way.
The problem is stated in the general framework of a non static flow in the vicinity of a catalytic and non porous surface (without aging). It is shown that the exact and systematic resolution method based on the Laplace transform, introduced previously by the author to model collisions in the gas phase, can be extended to the present problem. The proposed approach is applied to the modelling of the Eley-Rideal and Langmuir-Hinshelwood recombinations, assuming that the coverage is locally at equilibrium. The models are developed considering one atomic species and extended to the general case of several atomic species. Numerical calculations show that the models derived in this way reproduce with accuracy behaviors observed experimentally.
(24 S., 1998)

8. J. Ohser, B. Steinbach, C. Lang

Efficient Texture Analysis of Binary Images

A new method of determining some characteristics of binary images is proposed based on a special linear filtering. This technique enables the estimation of the area fraction, the specific line length, and the specific integral of curvature. Furthermore, the specific length of the total projection is obtained, which gives detailed information about the texture of the image. The influence of lateral and directional resolution depending on the size of the applied filter mask is discussed in detail. The technique includes a method of increasing directional resolution for texture analysis while keeping lateral resolution as high as possible.
(17 S., 1998)

9. J. Orlik

Homogenization for viscoelasticity of the integral type with aging and shrinkage

A multi-phase composite with periodic distributed inclusions with a smooth boundary is considered in this contribution. The composite component materials are supposed to be linear viscoelastic and aging (of the non-convolution integral type, for which the Laplace transform with respect to time is not effectively applicable) and are subjected to isotropic shrinkage. The free shrinkage deformation can be considered as a fictitious temperature deformation in the behavior law. The procedure presented in this paper proposes a way to determine average (effective homogenized) viscoelastic and shrinkage (temperature) composite properties and the homogenized stress-field from known properties of the

components. This is done by the extension of the asymptotic homogenization technique known for pure elastic non-homogeneous bodies to the non-homogeneous thermo-viscoelasticity of the integral non-convolution type. Up to now, the homogenization theory has not covered viscoelasticity of the integral type.
Sanchez-Palencia (1980), Francfort & Suquet (1987) (see [2], [9]) have considered homogenization for viscoelasticity of the differential form and only up to the first derivative order. The integral-modeled viscoelasticity is more general then the differential one and includes almost all known differential models. The homogenization procedure is based on the construction of an asymptotic solution with respect to a period of the composite structure. This reduces the original problem to some auxiliary boundary value problems of elasticity and viscoelasticity on the unit periodic cell, of the same type as the original non-homogeneous problem. The existence and uniqueness results for such problems were obtained for kernels satisfying some constrain conditions. This is done by the extension of the Volterra integral operator theory to the Volterra operators with respect to the time, whose 1 kernels are space linear operators for any fixed time variables. Some ideas of such approach were proposed in [11] and [12], where the Volterra operators with kernels depending additionally on parameter were considered. This manuscript delivers results of the same nature for the case of the space-operator kernels.
(20 S., 1998)

10. J. Mohring

Helmholtz Resonators with Large Aperture

The lowest resonant frequency of a cavity resonator is usually approximated by the classical Helmholtz formula. However, if the opening is rather large and the front wall is narrow this formula is no longer valid. Here we present a correction which is of third order in the ratio of the diameters of aperture and cavity. In addition to the high accuracy it allows to estimate the damping due to radiation. The result is found by applying the method of matched asymptotic expansions. The correction contains form factors describing the shapes of opening and cavity. They are computed for a number of standard geometries. Results are compared with numerical computations.
(21 S., 1998)

11. H. W. Hamacher, A. Schöbel

On Center Cycles in Grid Graphs

Finding "good" cycles in graphs is a problem of great interest in graph theory as well as in locational analysis. We show that the center and median problems are NP hard in general graphs. This result holds both for the variable cardinality case (i.e. all cycles of the graph are considered) and the fixed cardinality case (i.e. only cycles with a given cardinality p are feasible). Hence it is of interest to investigate special cases where the problem is solvable in polynomial time.
In grid graphs, the variable cardinality case is, for instance, trivially solvable if the shape of the cycle can be chosen freely.
If the shape is fixed to be a rectangle one can analyze rectangles in grid graphs with, in sequence, fixed dimension, fixed cardinality, and variable cardinality. In all cases a complete characterization of the optimal cycles and closed form expressions of the optimal objective values are given, yielding polynomial time algorithms for all cases of center rectangle problems.
Finally, it is shown that center cycles can be chosen as rectangles for small cardinalities such that the center cycle problem in grid graphs is in these cases completely solved.
(15 S., 1998)

12. H. W. Hamacher, K.-H. Küfer

Inverse radiation therapy planning - a multiple objective optimisation approach

For some decades radiation therapy has been proved successful in cancer treatment. It is the major task of clinical radiation treatment planning to realize on the one hand a high level dose of radiation in the cancer tissue in order to obtain maximum tumor control. On the other hand it is obvious that it is absolutely necessary to keep in the tissue outside the tumor, particularly in organs at risk, the unavoidable radiation as low as possible.
No doubt, these two objectives of treatment planning - high level dose in the tumor, low radiation outside the tumor - have a basically contradictory nature. Therefore, it is no surprise that inverse mathematical models with dose distribution bounds tend to be infeasible in most cases. Thus, there is need for approximations compromising between overdosing the organs at risk and underdosing the target volume.
Differing from the currently used time consuming iterative approach, which measures deviation from an ideal (non-achievable) treatment plan using recursively trial-and-error weights for the organs of interest, we go a new way trying to avoid a priori weight choices and consider the treatment planning problem as a multiple objective linear programming problem: with each organ of interest, target tissue as well as organs at risk, we associate an objective function measuring the maximal deviation from the prescribed doses.
We build up a data base of relatively few efficient solutions representing and approximating the variety of Pareto solutions of the multiple objective linear programming problem. This data base can be easily scanned by physicians looking for an adequate treatment plan with the aid of an appropriate online tool.
(14 S., 1999)

13. C. Lang, J. Ohser, R. Hilfer

On the Analysis of Spatial Binary Images

This paper deals with the characterization of microscopically heterogeneous, but macroscopically homogeneous spatial structures. A new method is presented which is strictly based on integral-geometric formulae such as Crofton's intersection formulae and Hadwiger's recursive definition of the Euler number. The corresponding algorithms have clear advantages over other techniques. As an example of application we consider the analysis of spatial digital images produced by means of Computer Assisted Tomography.
(20 S., 1999)

14. M. Junk

On the Construction of Discrete Equilibrium Distributions for Kinetic Schemes

A general approach to the construction of discrete equilibrium distributions is presented. Such distribution functions can be used to set up Kinetic Schemes as well as Lattice Boltzmann methods. The general principles are also applied to the construction of Chapman Enskog distributions which are used in Kinetic Schemes for compressible Navier-Stokes equations.
(24 S., 1999)

15. M. Junk, S. V. Raghurame Rao

A new discrete velocity method for Navier-Stokes equations

The relation between the Lattice Boltzmann Method, which has recently become popular, and the Kinetic Schemes, which are routinely used in Computational Fluid Dynamics, is explored. A new discrete velocity model for the numerical solution of Navier-Stokes equations for incompressible fluid flow is presented by combining both the approaches. The new scheme can be interpreted as a pseudo-compressibility method and, for a particular choice of parameters, this interpretation carries over to the Lattice Boltzmann Method.
(20 S., 1999)

16. H. Neunzert

Mathematics as a Key to Key Technologies

The main part of this paper will consist of examples, how mathematics really helps to solve industrial problems; these examples are taken from our Institute for Industrial Mathematics, from research in the Technomathematics group at my university, but also from ECMI groups and a company called TecMath, which originated 10 years ago from my university group and has already a very successful history.
(39 S. (vier PDF-Files), 1999)

17. J. Ohser, K. Sandau

Considerations about the Estimation of the Size Distribution in Wicksell's Corpuscle Problem

Wicksell's corpuscle problem deals with the estimation of the size distribution of a population of particles, all having the same shape, using a lower dimensional sampling probe. This problem was originary formulated for particle systems occurring in life sciences but its solution is of actual and increasing interest in materials science. From a mathematical point of view, Wicksell's problem is an inverse problem where the interesting size distribution is the unknown part of a Volterra equation. The problem is often regarded ill-posed, because the structure of the integrand implies unstable numerical solutions. The accuracy of the numerical solutions is considered here using the condition number, which allows to compare different numerical methods with different (equidistant) class sizes and which indicates, as one result, that a finite section thickness of the probe reduces the numerical problems. Furthermore, the relative error of estimation is computed which can be split into two parts. One part consists of the relative discretization error that increases for increasing class size, and the second part is related to the relative statistical error which increases with decreasing class size. For both parts, upper bounds can be given and the sum of them indicates an optimal class width depending on some specific constants.
(18 S., 1999)

18. E. Carrizosa, H. W. Hamacher, R. Klein, S. Nickel

Solving nonconvex planar location problems by finite dominating sets

It is well-known that some of the classical location problems with polyhedral gauges can be solved in polynomial time by finding a finite dominating set, i. e. a finite set of candidates guaranteed to contain at least one optimal location.
In this paper it is first established that this result holds for a much larger class of problems than currently considered in the literature. The model for which this result can be proven includes, for instance, location problems with attraction and repulsion, and location-allocation problems. Next, it is shown that the approximation of general gauges by polyhedral ones in the objective function of our general model can be analyzed with regard to the subsequent error in the optimal objective value. For the approximation problem two different approaches are described, the sandwich procedure and the greedy algorithm. Both of these approaches lead - for fixed epsilon - to polynomial approximation algorithms with accuracy epsilon for solving the general model considered in this paper.
Keywords:
Continuous Location, Polyhedral Gauges, Finite Dominating Sets, Approximation, Sandwich Algorithm, Greedy Algorithm
(19 S., 2000)

19. A. Becker

A Review on Image Distortion Measures

Within this paper we review image distortion measures. A distortion measure is a criterion that assigns a "quality number" to an image. We distinguish between mathematical distortion measures and those distortion measures in-cooperating a priori knowledge about the imaging devices (e. g. satellite images), image processing algorithms or the human physiology. We will consider representative examples of different kinds of distortion measures and are going to discuss them.
Keywords:
Distortion measure, human visual system
(26 S., 2000)

20. H. W. Hamacher, M. Labbé, S. Nickel, T. Sonneborn

Polyhedral Properties of the Uncapacitated Multiple Allocation Hub Location Problem

We examine the feasibility polyhedron of the uncapacitated hub location problem (UHL) with multiple allocation, which has applications in the fields of air passenger and cargo transportation, telecommunication and postal delivery services. In particular we determine the dimension and derive some classes of facets of this polyhedron. We develop some general rules about lifting facets from the uncapacitated facility location (UFL) for UHL and projecting facets from UHL to UFL. By applying these rules we get a new class of facets for UHL which dominates the inequalities in the original formulation. Thus we get a new formulation of UHL whose constraints are all facet–defining. We show its superior computational performance by benchmarking it on a well known data set.
Keywords:
integer programming, hub location, facility location, valid inequalities, facets, branch and cut
(21 S., 2000)

21. H. W. Hamacher, A. Schöbel

Design of Zone Tariff Systems in Public Transportation

Given a public transportation system represented by its stops and direct connections between stops, we consider two problems dealing with the prices for the customers: The fare problem in which subsets of stops are already aggregated to zones and "good" tariffs have to be found in the existing zone system. Closed form solutions for the fare problem are presented for three objective functions. In the zone problem the design of the zones is part of the problem. This problem is NP hard and we therefore propose three heuristics which prove to be very successful in the redesign of one of Germany's transportation systems.
(30 S., 2001)

22. D. Hietel, M. Junk, R. Keck, D. Teleaga:

The Finite-Volume-Particle Method for Conservation Laws

In the Finite-Volume-Particle Method (FVPM), the weak formulation of a hyperbolic conservation law is discretized by restricting it to a discrete set of test functions. In contrast to the usual Finite-Volume approach, the test functions are not taken as characteristic functions of the control volumes in a spatial grid, but are chosen from a partition of unity with smooth and overlapping partition functions (the particles), which can even move along prescribed velocity fields. The information exchange between particles is based on standard numerical flux functions. Geometrical information, similar to the surface area of the cell faces in the Finite-Volume Method and the corresponding normal directions are given as integral quantities of the partition functions.
After a brief derivation of the Finite-Volume-Particle Method, this work focuses on the role of the geometric coefficients in the scheme.
(16 S., 2001)

23. T. Bender, H. Hennes, J. Kalcsics, M. T. Melo, S. Nickel

Location Software and Interface with GIS and Supply Chain Management

The objective of this paper is to bridge the gap between location theory and practice. To meet this objective focus is given to the development of software capable of addressing the different needs of a wide group of users. There is a very active community on location theory encompassing many research fields such as operations research, computer science, mathematics, engineering, geography, economics and marketing. As a result, people working on facility location problems have a very diverse background and also different needs regarding the software to solve these problems. For those interested in non-commercial applications (e. g. students and researchers), the library of location algorithms (LoLA can be of considerable assistance. LoLA contains a collection of efficient algorithms for solving planar, network and discrete facility location problems. In this paper, a detailed description of the functionality of LoLA is presented. In the fields of geography and marketing, for instance, solving facility location problems requires using large amounts of demographic data. Hence, members of these groups (e. g. urban planners and sales managers) often work with geographical information too s. To address the specific needs of these users, LoLA was inked to a geographical information system (GIS) and the details of the combined functionality are described in the paper. Finally, there is a wide group of practitioners who need to solve large problems and require special purpose software with a good data interface. Many of such users can be found, for example, in the area of supply chain management (SCM). Logistics activities involved in strategic SCM include, among others, facility location planning. In this paper, the development of a commercial location software tool is also described. The too is embedded in the Advanced Planner and Optimizer SCM software developed by SAP AG, Walldorf, Germany. The paper ends with some conclusions and an outlook to future activities.
Keywords:
facility location, software development, geographical information systems, supply chain management.
(48 S., 2001)

24. H. W. Hamacher, S. A. Tjandra

Mathematical Modelling of Evacuation Problems: A State of Art

This paper details models and algorithms which can be applied to evacuation problems. While it concentrates on building evacuation many of the results are applicable also to regional evacuation. All models consider the time as main parameter, where the travel time between components of the building is part of the input and the overall evacuation time is the output. The paper distinguishes between macroscopic and microscopic evacuation models both of which are able to capture the evacuees' movement over time.
Macroscopic models are mainly used to produce good lower bounds for the evacuation time and do not consider any individual behavior during the emergency situation. These bounds can be used to analyze existing buildings or help in the design phase of planning a building. Macroscopic approaches which are based on dynamic network flow models (minimum cost dynamic flow, maximum dynamic flow, universal maximum flow, quickest path and quickest flow) are described. A special feature of the presented approach is the fact, that travel times of evacuees are not restricted to be constant, but may be density dependent. Using multicriteria optimization priority regions and blockage due to fire or smoke may be considered. It is shown how the modelling can be done using time parameter either as discrete or continuous parameter.
Microscopic models are able to model the individual evacuee's characteristics and the interaction among evacuees which influence their movement. Due to the corresponding huge amount of data one uses simulation approaches. Some probabilistic laws for individual evacuee's movement are presented. Moreover ideas to model the evacuee's movement using cellular automata (CA) and resulting software are presented.
In this paper we will focus on macroscopic models and only summarize some of the results of the microscopic approach. While most of the results are applicable to general evacuation situations, we concentrate on building evacuation.
(44 S., 2001)

25. J. Kuhnert, S. Tiwari

Grid free method for solving the Poisson equation

A Grid free method for solving the Poisson equation is presented. This is an iterative method. The method is based on the weighted least squares approximation in which the Poisson equation is enforced to be satisfied in every iterations. The boundary conditions can also be enforced in the iteration process. This is a local approximation procedure. The Dirichlet, Neumann and mixed boundary value problems on a unit square are presented and the analytical solutions are compared with the exact solutions. Both solutions matched perfectly.
Keywords:
Poisson equation, Least squares method, Grid free method
(19 S., 2001)

26. T. Götz, H. Rave, D. Reinel-Bitzer, K. Steiner, H. Tiemeier

Simulation of the fiber spinning process

To simulate the influence of process parameters to the melt spinning process a fiber model is used and coupled with CFD calculations of the quench air flow. In the fiber model energy, momentum and mass balance are solved for the polymer mass flow. To calculate the quench air the Lattice Boltzmann method is used. Simulations and experiments for different process parameters and hole configurations are compared and show a good agreement.
Keywords:
Melt spinning, fiber model, Lattice Boltzmann, CFD
(19 S., 2001)

27. A. Zemitis

On interaction of a liquid film with an obstacle

In this paper mathematical models for liquid films generated by impinging jets are discussed. Attention is stressed to the interaction of the liquid film with some obstacle. S. G. Taylor [Proc. R. Soc. London Ser. A 253, 313 (1959)] found that the liquid film generated by impinging jets is very sensitive to properties of the wire which was used as an obstacle. The aim of this presentation is to propose a modification of the Taylor's model, which allows to simulate the film shape in cases, when the angle between jets is different from 180°. Numerical results obtained by discussed models give two different shapes of the liquid film similar as in Taylors experiments. These two shapes depend on the regime: either droplets are produced close to the obstacle or not. The difference between two regimes becomes larger if the angle between jets decreases. Existence of such two regimes can be very essential for some applications of impinging jets, if the generated liquid film can have a contact with obstacles.
Keywords:
impinging jets, liquid film, models, numerical solution, shape
(22 S., 2001)

28. I. Ginzburg, K. Steiner

Free surface lattice-Boltzmann method to model the filling of expanding cavities by Bingham Fluids

The filling process of viscoplastic metal alloys and plastics in expanding cavities is modelled using the lattice Boltzmann method in two and three dimensions. These models combine the regularized Bingham model for viscoplastic with a free-interface algorithm. The latter is based on a modified immiscible lattice Boltzmann model in which one species is the fluid and the other one is considered as vacuum. The boundary conditions at the curved liquid-vacuum interface are met without any geometrical front reconstruction from a first-order Chapman-Enskog expansion. The numerical results obtained with these models are found in good agreement with available theoretical and numerical analysis.
Keywords:
Generalized LBE, free-surface phenomena, interface boundary conditions, filling processes, Bingham viscoplastic model, regularized models
(22 S., 2001)

29. H. Neunzert

»Denn nichts ist für den Menschen als Menschen etwas wert, was er nicht mit Leidenschaft tun kann«

Vortrag anlässlich der Verleihung des Akademiepreises des Landes Rheinland-Pfalz am 21.11.2001

Was macht einen guten Hochschullehrer aus? Auf diese Frage gibt es sicher viele verschiedene, fachbezogene Antworten, aber auch ein paar allgemeine Gesichtspunkte: es bedarf der »Leidenschaft« für die Forschung (Max Weber), aus der dann auch die Begeisterung für die Lehre erwächst. Forschung und Lehre gehören zusammen, um die Wissenschaft als lebendiges Tun vermitteln zu können. Der Vortrag gibt Beispiele dafür, wie in angewandter Mathematik Forschungsaufgaben aus praktischen Alltagsproblemstellungen erwachsen, die in die Lehre auf verschiedenen Stufen (Gymnasium bis Graduiertenkolleg) einfließen; er leitet damit auch zu einem aktuellen Forschungsgebiet, der Mehrskalenanalyse mit ihren vielfältigen Anwendungen in Bildverarbeitung, Materialentwicklung und Strömungsmechanik über, was aber nur kurz gestreift wird. Mathematik erscheint hier als eine moderne Schlüsseltechnologie, die aber auch enge Beziehungen zu den Geistes- und Sozialwissenschaften hat.
Keywords:
Lehre, Forschung, angewandte Mathematik, Mehrskalenanalyse, Strömungsmechanik
(18 S., 2001)

30. J. Kuhnert, S. Tiwari

Finite pointset method based on the projection method for simulations of the incompressible Navier-Stokes equations

A Lagrangian particle scheme is applied to the projection method for the incompressible Navier-Stokes equations. The approximation of spatial derivatives is obtained by the weighted least squares method. The pressure Poisson equation is solved by a local iterative procedure with the help of the least squares method. Numerical tests are performed for two dimensional cases. The Couette flow, Poiseuelle flow, decaying shear flow and the driven cavity flow are presented. The numerical solutions are obtained for stationary as well as instationary cases and are compared with the analytical solutions for channel flows. Finally, the driven cavity in a unit square is considered and the stationary solution obtained from this scheme is compared with that from the finite element method.
Keywords:
Incompressible Navier-Stokes equations, Meshfree method, Projection method, Particle scheme, Least squares approximation
AMS subject classification:
76D05, 76M28
(25 S., 2001)

31. R. Korn, M. Krekel

Optimal Portfolios with Fixed Consumption or Income Streams

We consider some portfolio optimisation problems where either the investor has a desire for an a priori specified consumption stream or/and follows a deterministic pay in scheme while also trying to maximize expected utility from final wealth. We derive explicit closed form solutions for continuous and discrete monetary streams. The mathematical method used is classical stochastic control theory.
Keywords:
Portfolio optimisation, stochastic control, HJB equation, discretisation of control problems.
(23 S., 2002)

32. M. Krekel

Optimal portfolios with a loan dependent credit spread

If an investor borrows money he generally has to pay higher interest rates than he would have received, if he had put his funds on a savings account. The classical model of continuous time portfolio optimisation ignores this effect. Since there is obviously a connection between the default probability and the total percentage of wealth, which the investor is in debt, we study portfolio optimisation with a control dependent interest rate. Assuming a logarithmic and a power utility function, respectively, we prove explicit formulae of the optimal control.
Keywords:
Portfolio optimisation, stochastic control, HJB equation, credit spread, log utility, power utility, non-linear wealth dynamics
(25 S., 2002)

33. J. Ohser, W. Nagel, K. Schladitz

The Euler number of discretized sets - on the choice of adjacency in homogeneous lattices

Two approaches for determining the Euler-Poincaré characteristic of a set observed on lattice points are considered in the context of image analysis { the integral geometric and the polyhedral approach. Information about the set is assumed to be available on lattice points only. In order to retain properties of the Euler number and to provide a good approximation of the true Euler number of the original set in the Euclidean space, the appropriate choice of adjacency in the lattice for the set and its background is crucial. Adjacencies are defined using tessellations of the whole space into polyhedrons. In R 3 , two new 14 adjacencies are introduced additionally to the

well known 6 and 26 adjacencies. For the Euler number of a set and its complement, a consistency relation holds. Each of the pairs of adjacencies (14:1; 14:1), (14:2; 14:2), (6; 26), and (26; 6) is shown to be a pair of complementary adjacencies with respect to this relation. That is, the approximations of the Euler numbers are consistent if the set and its background (complement) are equipped with this pair of adjacencies. Furthermore, sufficient conditions for the correctness of the approximations of the Euler number are given. The analysis of selected microstructures and a simulation study illustrate how the estimated Euler number depends on the chosen adjacency. It also shows that there is not a uniquely best pair of adjacencies with respect to the estimation of the Euler number of a set in Euclidean space.
Keywords: image analysis, Euler number, neighborhod relationships, cuboidal lattice
(32 S., 2002)

34. I. Ginzburg, K. Steiner
Lattice Boltzmann Model for Free-Surface flow and Its Application to Filling Process in Casting

A generalized lattice Boltzmann model to simulate free-surface is constructed in both two and three dimensions. The proposed model satisfies the interfacial boundary conditions accurately. A distinctive feature of the model is that the collision processes is carried out only on the points occupied partially or fully by the fluid. To maintain a sharp interfacial front, the method includes an anti-diffusion algorithm. The unknown distribution functions at the interfacial region are constructed according to the first order Chapman-Enskog analysis. The interfacial boundary conditions are satisfied exactly by the coefficients in the Chapman-Enskog expansion. The distribution functions are naturally expressed in the local interfacial coordinates. The macroscopic quantities at the interface are extracted from the least-square solutions of a locally linearized system obtained from the known distribution functions. The proposed method does not require any geometric front construction and is robust for any interfacial topology. Simulation results of realistic filling process are presented: rectangular cavity in two dimensions and Hammer box, Campbell box, Sheffield box, and Motorblock in three dimensions. To enhance the stability at high Reynolds numbers, various upwind-type schemes are developed. Free-slip and no-slip boundary conditions are also discussed.
Keywords: Lattice Boltzmann models; free-surface phenomena; interface boundary conditions; filling processes; injection molding; volume of fluid method; interface boundary conditions; advection-schemes; upwind-schemes
(54 S., 2002)